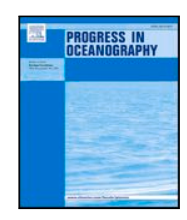


Contents lists available at ScienceDirect

Progress in Oceanography

journal homepage: www.elsevier.com/locate/pocean





Global observations of submesoscale coherent vortices in the ocean

Daniel McCoy*, Daniele Bianchi, Andrew L. Stewart

Department of Atmospheric and Oceanic Sciences, University of California - Los Angeles, 520 Portola Plaza, Los Angeles, CA 90095, USA

ARTICLE INFO

Keywords: Argo floats Mesoscale eddies Ocean transport Water masses Volume transport Water mixing

ABSTRACT

Subsurface-intensified anticyclones are ubiquitous in the ocean, yet their impact on the large-scale transport of heat, salt and chemical tracers is poorly understood. These submesoscale coherent vortices (SCVs) can trap and advect waters thousands of kilometers away from the formation region, providing a transport pathway that is unresolved by low-resolution Earth System Models. However, knowledge of the importance of these eddies for the large scale circulation is hindered by the lack of systematic observations. Here, we take advantage of the global network of Argo floats to identify occurrences of these eddies, which appear as weakly stratified anomalous water masses with Gaussian-shaped vertical structures. We develop a general algorithm to detect subsurface eddies that have propagated away from their source region, and apply it to the database of Argo float profiles, resulting in roughly 4000 detections from more than 20 years of observations. We further group detections into regional populations to identify hot-spots of generation and mechanisms of formation. Analysis of regional SCV statistics reveals important sites of SCV generation in Eastern Boundary Upwelling Systems, marginal sea overflows, and mode water formation regions along major open-ocean fronts. Because of the heat and salt anomaly contained within their cores, SCV could leave a significant imprint on the hydrographic properties of water masses in regions of high SCV density.

1. Introduction

Anticyclonic oceanic eddies with subsurface velocity maxima populate many areas of the world ocean and exert a regional influence on heat, salt, and nutrient transport (Richardson et al., 2000; Nauw et al., 2006; Pegliasco et al., 2015; Frenger et al., 2018). They have been detected within the near-surface, intermediate, and near-bottom layers of the ocean, and are characterized by horizontal scales that range from the submesoscale (<10 km) to the internal Rossby radius of deformation (10-100 km) (McWilliams, 1985; D'Asaro, 1988; Nauw et al., 2006; Molemaker et al., 2015). A defining characteristic of these eddies is the doming and bowling of isopycnal surfaces around a weakly stratified, gradient-wind balanced water mass (McWilliams, 1985; Gordon et al., 2002; Nauw et al., 2006) that also exhibits anomalously low potential vorticity (PV) (Meunier et al., 2018). Intrathermocline eddies (ITEs) are variants that displace the main thermocline and are thought to be generated by a variety of mechanisms that include: (1) subduction of mode waters at frontal boundaries (Spall, 1995; Hogan and Hurlburt, 2011); (2) isolation of pre-existing mesoscale anticyclones from the surface by advection or restratification (Hogan and Hurlburt, 2011); (3) a reduction of PV along fronts by counter-directional winds on the frontal jet (Thomas et al., 2009); (4) intense local upwelling driven by eddywind interactions that induces isopycnal doming (McGillicuddy, 2014).

Sub-thermocline variants common to eastern boundary upwelling systems (EBUS) are frequently termed submesoscale coherent vortices (SCVs, McWilliams, 1985). They have been shown to be primarily generated via subsurface currents that undergo flow separation near capes or promontories, followed by submesoscale instabilities and roll-up into coherent vortices (D'Asaro, 1988; Molemaker et al., 2015; Thomsen et al., 2016). Here we use the term SCV to describe both types of eddies, due to their similar dynamical structures and role in subsurface ocean circulation.

Interest in SCVs is motivated by their occasional propagation within or below the pycnocline, where relatively weak turbulent mixing allows for a slower decay compared to mesoscale eddies (McWilliams, 1985; Collins et al., 2013). Observations also suggest a preference for anticyclonic rotation and isolation of core water mass over many cycles due to the rapid rotation (McWilliams, 1985; Schütte et al., 2016). These characteristics allows for individual SCVs to exist for several years, while efficiently transporting nutrients and other material properties thousands of kilometers away from their formation regions (Richardson et al., 2000; Frenger et al., 2018). For example, Lukas and Santiago-Mandujano (2001) detected an SCV with a radius of at least 15 km to the North of the Hawaiian Islands that was virtually depleted in dissolved oxygen throughout its core. The highly atypical hydrographic

E-mail address: demccoy@atmos.ucla.edu (D. McCoy).

^{*} Corresponding author.

properties within the eddy relative to the surrounding water suggested formation off the southern tip of Baja California several years prior to detection.

The long lifetimes and unique dynamics of SCVs suggest that they are important in shaping the distribution and variability of heat, salt, and biogeochemical tracers over large swaths of the ocean. Notably, compared to surface intensified eddies, SCVs differ strongly in both their efficiency in carrying water mass anomalies, and the resulting biogeochemical responses within the encapsulated waters (Schütte et al., 2016). A study by Frenger et al. (2018) used a global eddying ocean biogeochemical model to suggest that SCVs shed from Pacific EBUS accounted for roughly 10% of the offshore transport of nutrients from those systems along the isopycnals where eddies are found, while Pelland et al. (2013) estimated that up to 44% of the heat and salt loss from the California undercurrent is a result of SCV generation along its pathway. Perhaps most striking are the Mediterranean outflow eddies or 'Meddies' that appear in the North Atlantic Ocean as blobs of dense, salty, weakly stratified Mediterranean Sea water (McWilliams, 1985; Bower et al., 1997; Richardson et al., 2000; Barbosa Aguiar et al., 2013; Bashmachnikov et al., 2015). Settling to around 1000 m before adjusting and acquiring their characteristic anticyclonic rotation, they could account for roughly 40% of the Mediterranean outflow, and contribute to the westward salinity flux within the Mediterranean salt tongue (McWilliams, 1985; Richardson et al., 2000). Additionally, the isolation of SCV core properties may also establish a distinct biogeochemical environment and subsequent biological community compared with the surrounding waters (Löscher et al., 2015; Frenger et al., 2018). Low-oxygen SCVs, such as those shed from EBUS, have been shown to be hot-spots of fixed nitrogen losses and production of nitrous oxide, a powerful greenhouse gas (Altabet et al., 2012; Arévalo-Martínez et al., 2015; Löscher et al., 2015; Grundle et al., 2017).

After propagation from source regions, the core properties of SCVs often strongly contrast with surrounding waters, allowing easy detection as vertically confined, weakly stratified, Gaussian-shaped water mass anomalies (Simpson et al., 1984; McWilliams, 1985; Zhang et al., 2015). Examples from the observational record include California Undercurrent 'Cuddies' (Garfield et al., 1999; Chaigneau et al., 2011; Pelland et al., 2013; Collins et al., 2013), Peru-Chile 13 °C Water Eddies (Johnson and McTaggart, 2010; Chaigneau et al., 2011; Hormazabal et al., 2013), Labrador Sea outflow eddies (Bower et al., 2013), Beaufort Sea eddies (D'Asaro, 1988; Zhao et al., 2018), Persian Gulf eddies (L'Hégaret et al., 2016), Red Sea outflow eddies (Shapiro and Meschanov, 1991), and the ITE's of the Northwest Pacific (Gordon et al., 2002; Hogan and Hurlburt, 2011; Zhang et al., 2015) and Southern Indian (Nauw et al., 2006; Dilmahamod et al., 2018) Oceans. Yet, despite the multitude of studies documenting individual SCV populations, their global occurrence, properties, and generation frequency remain poorly constrained.

While the advent of satellite altimetric observations facilitated the study of surface-intensified eddies (Chelton et al., 1998; Chaigneau et al., 2011; Gaube et al., 2018), the weak or undetectable sea-surface signature of SCVs restricts their observational record to mostly chance encounters with shipboard instrumentation or autonomous sampling platforms. Over the past two decades, the global array of roughly 4000 operational Argo floats has produced nearly 2 million hydrographic profiles of the upper 2000 meters of the ocean, offering a unique opportunity to study SCVs. This vast number of profiles provides robust estimates of regional climatological water column properties, which can be exploited to detect SCVs based on their anomalous hydrographic signatures (Johnson and McTaggart, 2010; Pegliasco et al., 2015; Zhang et al., 2015; Li et al., 2017).

In this paper, we develop a general algorithm to identify Argo float profiles that crossed the interior of SCVs, expanding similar methods used by Johnson and McTaggart (2010) and Zhang et al. (2015) to study regional SCV populations. Based on theory and observations, we identify SCVs within Argo profiles using three primary criteria.

First, a SCV must contain a vertically confined, Gaussian-shaped water mass anomaly, indicative of remote subsurface advection. Second, the water mass anomaly must be weakly stratified, corresponding to doming/bowling of isopycnals above and below the water mass, respectively. Finally, horizontal velocities estimated from hydrographic properties must suggest a local maxima within the range of the SCV. We establish specific detection criteria corresponding to these conditions, based on: (1) spiciness, a measure of density-compensated thermohaline variability, (2) buoyancy frequency, a measure of the vertical stratification, and (3) dynamic height anomaly, a measure of the horizontal pressure gradient force.

By applying the algorithm to the global Argo array, we detect roughly 4000 "spicy-core" SCVs (anomalously warm and salty) and "minty-core" SCVs (anomalously cold and fresh). We analyze the properties of these detections to shed light on the regional variability and generation mechanisms of SCVs, and their impacts on heat and salt distribution. The rest of the paper is organized as follows: Section 2 discusses the Argo data set and the algorithm used to detect SCVs; Section 3 describes the global and regional results after application of the detection method; Section 4 discusses possible generation mechanisms associated with large coherent populations of SCV detections; and Section 5 provides estimates of their numbers and expected contribution to heat and salt budgets globally.

2. Methods

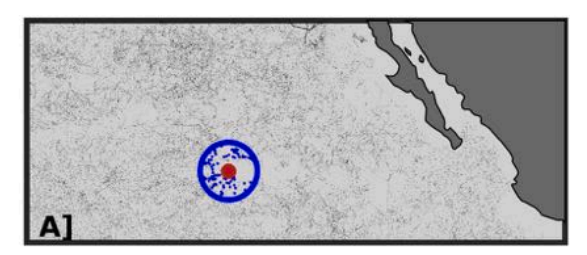
2.1. Data and quality control

We downloaded Argo float profiles from August 1997 to January 2020 from the U.S. Argo global data center (GDAC). Vertical levels without 'good' or 'probably good' quality control flags were rejected, and delayed-mode or adjusted values were used whenever available. Questionable float profiles based on a list provided by the GDAC ('grey-listed' floats) were removed. We further applied the following quality control criteria to remove casts with poor vertical resolution. We rejected casts that did not contain data from 0 to 100 dbar, or data greater than 700 dbar; profiles with vertical spacing greater than 65 dbar between 100-700 dbar were also excluded. Of the profiles that passed these criteria, any data between 0-1000 dbar were accepted until the difference between pressure levels was greater than 65 dbar. For the casts deeper than 1000 dbar, a 105 dbar resolution threshold was applied past that point. Finally, profiles were removed if they contained less than 40 vertical levels, or if they contained potential density inversions below the mixed layer (defined by the depth where potential density exceeds the surface value by 0.03 kg m⁻³, de Boyer Montégut et al., 2004).

Of the initial 1,992,246 float profiles, 336,861 (17%) were rejected based on these criteria (Figure C.1). Quality controlled temperature and salinity profiles were then linearly interpolated to a 10 dbar pressure grid from 0 to 2000 dbar, before deriving spiciness, absolute salinity, conservative temperature, and potential density. Derived buoyancy frequency (N^2) profiles on the 10 dbar grid were found to contain significant small-scale noise. To minimize this noise, we derived buoyancy frequency profiles from temperature and salinity profiles that were interpolated to a finer 2 dbar grid and smoothed with a Gaussian filter with a bandwidth of 10 dbar, before interpolating them back to the 10 dbar grid.

2.2. Anomalous water mass detection

To identify water mass anomalies associated with remotely-generated SCVs, we compared each profile with the nearest monthly climatological profile from the Roemmich–Gilson Argo Climatology (Roemmich and Gilson, 2009). In order to better preserve water mass properties, we derived and interpolated climatological profiles of spiciness and buoyancy frequency to each cast potential density, before



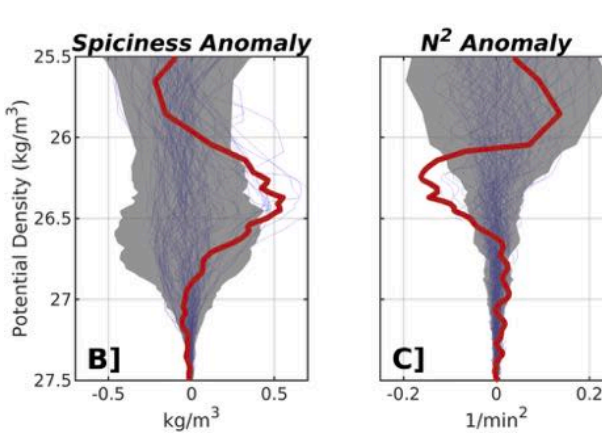


Fig. 1. Example of Argo cast exceeding spiciness and buoyancy frequency anomaly thresholds for SCV detection. (A) Locations of Argo float 4900860, cycle 347 (thick red point), and all floats within a 220 km radius circle that were conducted within \pm 45 days of the cast date, regardless of year (blue points); all other Argo casts are shown as faint gray dots. (B) Spiciness anomaly versus potential density for both the cast (red curve) and the nearby comparable Argo casts (blue curves). Shaded gray regions represent calculated IQR thresholds along each isopycnal. (C) Same as (B), but for squared buoyancy frequency anomaly. Note the thresholds being exceeded in both plots at a density of roughly 26.4 kg m $^{-3}$. (For interpretation of the references to color in this figure legend, the reader is referred to the web version of this article.)

subtracting them to obtain anomaly profiles along isopycnals. We chose to subtract properties along density rather than pressure because of to the preferential movement of water masses along isopycnal surfaces (Talley et al., 2011). When climatological temperature or salinity profiles were not available at the cast location (such as near the coast), we computed an average climatological profile using data from neighboring cells. Float profiles that could not be paired with climatological profiles were excluded (Figure C.1).

To quantify the water mass variability at each profile location, we gathered spiciness and buoyancy frequency anomalies from all profiles conducted within 220 km of the cast coordinates that were also conducted within +-45 days of the cast date, regardless of year (Fig. 1A). We then calculated the interquartile range (IQR), or the difference between the 75th and 25th percentile, to quantify the statistical spread of anomalies at each density level. These spatial and temporal thresholds are similar to those applied in Pegliasco et al. (2015), and were chosen to prevent false detections in regions with large horizontal temperature and salinity gradients and/or significant seasonal variability. Profiles without at least 60 comparable casts fitting the above criteria were excluded. After organizing all values into percentiles, we defined upper and lower outlier thresholds at each density level as the 75% value plus 1.5 times the IQR, and the 25% value minus 1.5 times the IQR, respectively (Tukey, 1977). We analyzed IQR statistical thresholds rather than mean and standard deviations because the IQR is less sensitive to large outliers.

The upper and lower IQR thresholds in spiciness anomaly were applied to identify isopycnal surfaces with anomalously high or low spiciness, which we labeled as spicy (anomalously warm and salty) or minty (anomalously cold and fresh) water mass intrusions, respectively (shaded regions in Fig. 1B). Likewise, lower IQR thresholds in buoyancy

frequency anomaly (Fig. 1C) were used to identify anomalously weak stratification within the core of each intrusion (Section 2.4). While the 25% and 75% IQR threshold limits are commonly applied in statistical outlier detection (Tukey, 1977), they are rather restrictive. Thus, weakly stratified water mass intrusions detected using these thresholds likely represent an underestimate of their true number in the ocean. However, adopting these strict criteria provides the benefit of reducing false positives, thus generating robust detections that can be confidently attributed to SCV identification.

To avoid detecting surface features such as mesoscale eddies, we limit our detection routine to subsurface isopycnals only. Since SCVs have been previously identified within or below the upper pycnocline (here defined as the vertical level of greatest stratification), we restricted our search to isopycnals below this depth. To estimate this level at each cast location, we used the depth of maximum climatological N^2 (Figure C.2), a criterion that robustly isolated isopycnals near the surface with very large IQR. Any cast which featured at least two consecutive isopycnal surfaces below this depth, spaced apart by 10 dbar, which exceeded either of the spiciness thresholds discussed above was kept for further analysis.

2.3. Gaussian model fit

In order to detect the presence of anomalously weak stratification associated with spicy or minty water mass intrusions, we required an estimate of the vertical thickness of each intrusion. Since observations of SCVs suggest that their vertical structure is well represented by a Gaussian monopole (McWilliams, 1985; Pelland et al., 2013), to estimate the vertical thickness or extent H we fit a one-term Gaussian model to spiciness anomaly profiles (calculated along isopycnals) in pressure space of the form:

$$Ae^{-\left(\frac{z-z_o}{h}\right)^2},\tag{1}$$

where A is the maximum absolute spiciness anomaly exceeding the IQR threshold, z is the pressure profile, z_0 is the pressure of A, and h is the scale height. By fitting the model, we set H to be the distance encompassed by $z_0 \pm 2$ standard deviations (σ) of the Gaussian model:

$$H = 4\sigma = 2\sqrt{2}h. \tag{2}$$

To find the best fit of the Gaussian model to the spiciness anomaly profile, we allowed A to vary by $\pm 20\%$, H to vary between 100-1200 dbar, and z_0 to vary by $\pm 20\%$ of H. We then calculated the sum of squared residuals for all combinations by reducing the vertical spiciness anomaly profile to within each estimated H. After careful inspection of fit solutions, we only considered combinations where: (1) the squared two-dimensional correlation coefficient (R^2) between the reduced profile and model was greater than 0.5; (2) the root-meansquared error normalized to the min/max of the reduced spiciness profiles (NRMSE hereafter) was less than 0.5; (3) profile data exists within the extent of the predicted H; and (4) A was greater than 0.1 kg m⁻³. We chose the best combination in a least-square sense to estimate H, while simultaneously rejecting profiles which could not fit the above parameters or thresholds (purple dashed curve in Fig. 2B). In practice, this eliminated intrusions that were (1) not well represented by a vertical Gaussian structure, (2) too thin (< 100 dbar), or (3) too thick (>1200 dbar) and thus not likely to be a result of an SCV.

2.4. Weakly stratified core detection

After successfully fitting Gaussian curves to spicy and minty intrusions, we sought anomalously weak stratification within the vertical extent of each water mass, indicative of bowling/doming of isopycnals around the intrusion. However, inspection of profiles which succeeded in fitting the model occasionally revealed noisy signatures in buoyancy

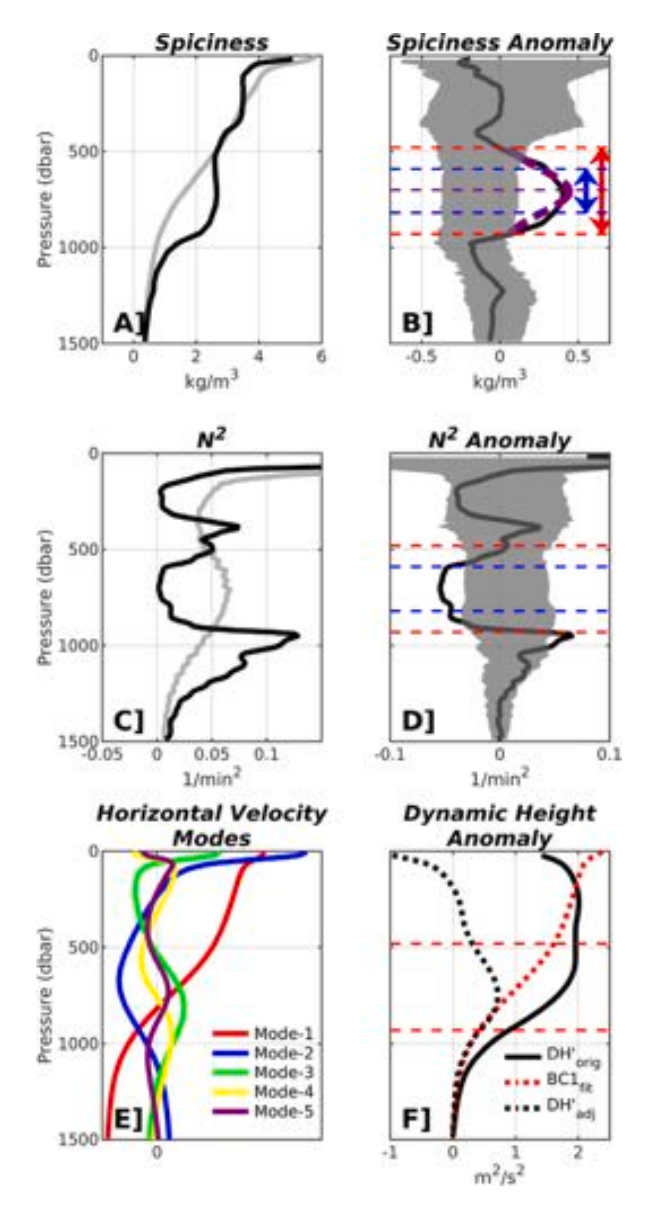


Fig. 2. (A) Spiciness versus pressure from Argo cast 69027, cycle 151 (black curve), and its local Argo climatology (gray curve). (B) Spiciness anomaly (derived along isopycnals) versus pressure (black curve) and the Gaussian model result (purple dashed curve). Dashed red lines represent estimates of the vertical thickness of the SCV, whereas dashed blue lines represent estimates of the SCV core thickness. The dashed purple line represents the estimate of the SCV core isopycnal/pressure. Shaded gray regions represent IQR thresholds used for the detection. (C,D) Same as (A,B), but for squared buoyancy frequency and squared buoyancy frequency anomaly. (E) The first five baroclinic horizontal velocity modes (dimensionless) vs. pressure, calculated from the climatological buoyancy frequency profile. (F) Original dynamic height anomaly (solid black curve), the first baroclinic horizontal velocity mode fit (dashed red curve), and the final adjusted dynamic height anomaly profile (dashed black curve). (For interpretation of the references to color in this figure legend, the reader is referred to the web version of this article.)

frequency anomaly along isopycnals. Since the weak stratification characteristic of SCVs should be most evident within waters just above and below the core of the feature, we defined an additional core vertical thickness or extent ($H_{\rm core}$) using the σ value from the Gaussian fitting routine:

$$H_{\rm core} = 2\sigma = \sqrt{2}h. \tag{3}$$

Using the above estimate, we set two strict criteria to check for weak stratification. First, the buoyancy frequency anomaly profile must be less than the lower N^2 IQR threshold at a depth within the core limits,

to represent the abnormally low stratification associated with SCVs. Second, the vertical mean of N^2 anomaly within this range must also be less than zero to avoid false detections due to occasionally noisy signals (e.g. Fig. 2D). Profiles that did not fit the above stratification criteria were rejected.

2.5. Subsurface velocity maxima detection

Satisfying the interior horizontal velocity maxima criteria is difficult without in-situ subsurface current data. However, the dynamic height differences between two nearby casts can be used as an estimate for the geostrophic velocity streamfunction, assuming flow at depth is relatively weak compared to surface velocities; note that this is a poor assumption within the vicinity of boundary currents and the Antarctic Circumpolar Current (ACC) (Ollitrault and Colin de Verdière, 2014). We take advantage of the fact that the majority (86%) of quality controlled floats began their casts at depths greater than 1000 dbar, where horizontal velocities are usually small (Talley et al., 2011). To test for a local extremum in the horizontal velocity, we calculated the dynamic height profile vs. pressure for both the detected SCV profile and the local Argo climatological profile. We started this calculation from the greatest cast pressure $p_{\rm ref}$, with the dynamic height anomaly $DH_0'(z)$ defined as the difference along isobars between the two profiles:

$$DH_{o}'(z) = \left(-\frac{1}{g} \int_{p_{\text{ref}}}^{p_{z}} \frac{1}{\rho_{\text{cast}}} dp\right) - \left(-\frac{1}{g} \int_{p_{\text{ref}}}^{p_{z}} \frac{1}{\rho_{\text{clim}}} dp\right). \tag{4}$$

We translated our velocity maximum criterion into finding a peak in $DH_0'(z)$ (i.e. geostrophic streamfunction) within the vertical extent estimate provided by the Gaussian model. Initial results indicated that slight misplacements of the pycnocline in pressure space between the SCV and the climatological profile can lead to large dynamic height anomalies along isobars, which dominated any SCV dynamic signature within the profile. This finding is not surprising given that, away from oceanic margins, the vertical structure of the ocean is almost entirely described by the barotropic and first baroclinic modes (Wunsch, 1997; Szuts et al., 2012). Thus, heaving caused by internal wave motions is an additional source of error in the dynamic height anomaly calculation.

To isolate and remove the impact of first baroclinic mode structures, we decomposed the climatological profile into vertical modes following Gill (1982) and Chelton et al. (1998). Briefly, we solved for the linear dynamical modes brought about by the standard eigenvalue problem of internal wave theory, using a Matlab routine written by Klink [1999]. We extracted the first baroclinic horizontal velocity mode (ψ_{BC1}) produced by the routine (e.g. Fig. 2E) and estimated the corresponding modal amplitude (α_{BC1}) by restricting the modal structure to be zero at p_{ref} , before applying a non-linear least-squares optimization to solve for the best fit to the dynamic height anomaly profile. To avoid over-fitting the BC1 projection to $DH'_0(z)$ profile sections with large SCV dynamic signatures, we ignored data between the vertical extent of the SCV in pressure space, as well as data within the mixed layer. Thus, the dynamic height anomaly attributed to first baroclinic mode structures and the adjusted dynamic height anomaly used for detection purposes are respectively defined as:

$$DH'_{BC1}(z) = \alpha_{BC1} \psi_{BC1}(z), \tag{5a}$$

$$DH'_{adi}(z) = DH'_{0}(z) - DH'_{RC1}(z).$$
 (5b)

In practice, the above method performed well in removing large runaway dynamic height anomalies when they appeared in the record by filtering out the impact of first baroclinic mode structures (e.g. Fig. 2F). However, baroclinic modes are likely an imperfect distinction between SCV structures and other mesoscale flows. Thus, removing the first mode component may delete part of the SCV structure. Our restriction to subsurface-intensified eddies suggests this is only a minor component of the circulation, and we note that the majority of profiles were largely unaffected by this approach (Figure C.3). A more

in-depth analysis of our strategy with dedicated SCVs observations would help refine this method further. We used the adjusted dynamic height anomaly $(DH'_{\rm adj}(z))$ to test for the presence of a local peak in dynamic height anomaly within the vertical extent of each intrusion, rejecting any profiles which did not exhibit this feature, while defining those that passed all the above criteria as spicy or minty-core SCVs.

2.6. SCV characterization

Previous studies suggest that the SCV radius is comparable to their internal Rossby deformation radius (McWilliams, 1985; Pelland et al., 2013; Zhang et al., 2015). Following the methods of Dewar and Meng (1995) and Zhang et al. (2015), we used estimates of SCV scale height (h, converted from dbar to m), core-isopycnal background buoyancy frequency ($N_{\rm clim}$), and the local Coriolis parameter (f) for each detected SCV to infer the first baroclinic deformation radius and thus an idealized horizontal scale L, defined as:

$$L = \frac{N_{\text{clim}}h}{f} \,. \tag{6}$$

While for some cases the above calculation represents the upper-limit of SCV length scales (McWilliams, 1985; Pelland et al., 2013), results from Zhang et al. (2015) and Li et al. (2017) suggest this is a realistic estimate.

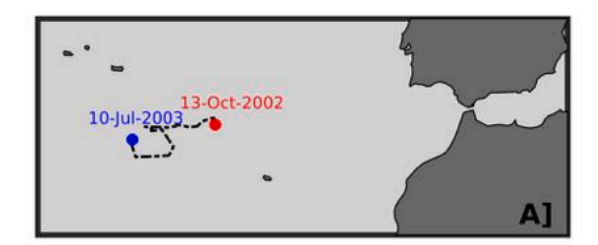
We note that the above estimates of h and L do not strongly depend on the assumption that each Argo float profile perfectly pierced the SCV through its center, which is likely false for most cases. Insofar as the three-dimensional SCV shape can be described by separate functions in the vertical and horizontal directions (McWilliams, 1985), the vertical SCV scale h will not depend on the distance of the profile from the eddy center. Likewise, our estimate of the horizontal extent L of an eddy only invokes the background stratification $N_{\rm clim}$ as an additional quantity. However, we also note that our method does not include consideration of the threshold of detectability for SCVs based on individual profiles, which would be influenced by the strength of the SCV, and the position of each profile relative to the SCV core.

2.7. SCV time-series

After detecting SCVs using the above methods, inspection of initial results revealed several instances of individual Argo floats detecting SCVs over consecutive 10-day cycles, suggesting that repeat sampling of the same eddy may be common with Argo. This is not surprising given the Lagrangian nature of Argo floats when stationed at their parking depths, which is often at 1000 m and potentially within the dynamical influence of SCVs. To reduce over-counting when compiling regional statistics, we sorted SCVs according to their float identification and cycle numbers, and grouped detections until they were more than 2 cycles (~ 30 days) apart of each other. Doing so provided us with time-series of profiles through the same SCV (e.g. Fig. 3B-D). When gathering SCV statistics such as core isopycnal and vertical thickness, we used the average from all profiles within an individual time-series to represent the SCV in histograms and property maps (see Sections 3.1-3.4). Additionally, the locations and dates of consecutive profiles allow for an estimate of SCV drift direction and speed, which can be used to draw inferences regarding the influence of regional SCV populations.

3. Results

After application of the SCV detection algorithm to the global Argo array, we identify 2501 casts piercing spicy-core SCVs, and 1583 casts piercing minty-core SCVs over more than 20 years of available data (Fig. 4A). By grouping detections from consecutive Argo casts (see Section 2.7), we are able to record 383 spicy-core SCV time-series and 169 minty-core SCV time-series, reducing the number of unique SCVs to 1716 spicy-core and 1258 minty-core detections. Visual inspection



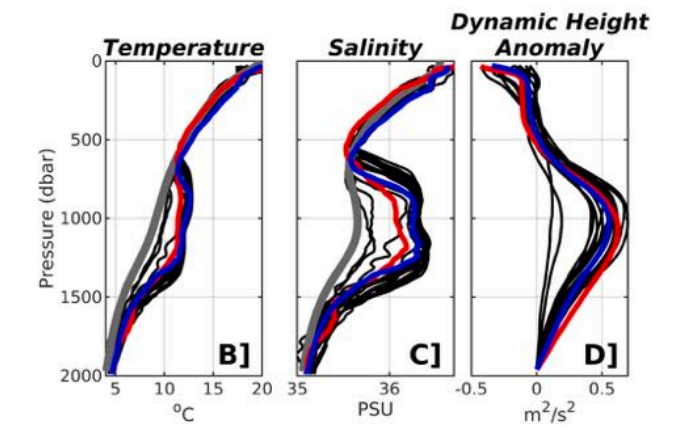


Fig. 3. (A) Locations of an example SCV time-series from Argo float 6900181, cycles 4–5, 8–12, 15, 18, 20, 22–28, 30–31 off of the northwest African coastline, with the first and final detection shown as red and blue circles. Panels B, C, and D show each casts' temperature, salinity, and dynamic height anomaly profile vs. pressure, respectively. Red and blue curves represent the initial and final casts, and thick gray curves in (B) and (C) show the averaged climatological profile from all casts. (For interpretation of the references to color in this figure legend, the reader is referred to the web version of this article.)

of their initial locations (Fig. 4B–E) reveals populations in every ocean basin; additionally, the correspondence between detected SCVs and previously identified Argo SCV populations such as those from Johnson and McTaggart (2010), Pegliasco et al. (2015), and Zhang et al. (2017) supports the detection criteria described in Section 2.2.

Spicy-core SCV detections generally outnumber minty-core detections throughout the subtropics and mid-latitudes, and vice-versa for high-latitude regions, as observed in the North Pacific and Southern Ocean. Maps of average core properties and vertical thickness estimates are shown in Figs. 5 and 6 for spicy-core and minty-core SCVs, respectively. Several regions show SCVs with similar hydrographic characteristics, such as widespread spicy-core populations in the Eastern Tropical Pacific, suggesting common formation mechanisms in those regions. In an effort to describe regional SCV variability and identify coherent populations, we divide each ocean into north and south basins, before further separating the eastern and western parts (i.e. Northeast Pacific, see black polygons in Fig. 4A). We also separate the Southern Ocean due to a high number of coherent minty-core SCV detections, by defining a region poleward of 40°S. We then construct histograms of SCV core statistics to facilitate property comparisons across and within basins. The following sections discuss SCV detections and their statistics organized by ocean basin, highlighting notable hotspots and coherent SCV populations wherever they appear. A more fine-grained characterization of our detections is further presented for reference in Appendix D.

3.1. Pacific SCVs

In the Northwest Pacific, we find 249 spicy-core SCVs spatially concentrated along the western boundary, ranging from the Philippine Islands to the east of Japan, up to the latitude of the Kuril Islands

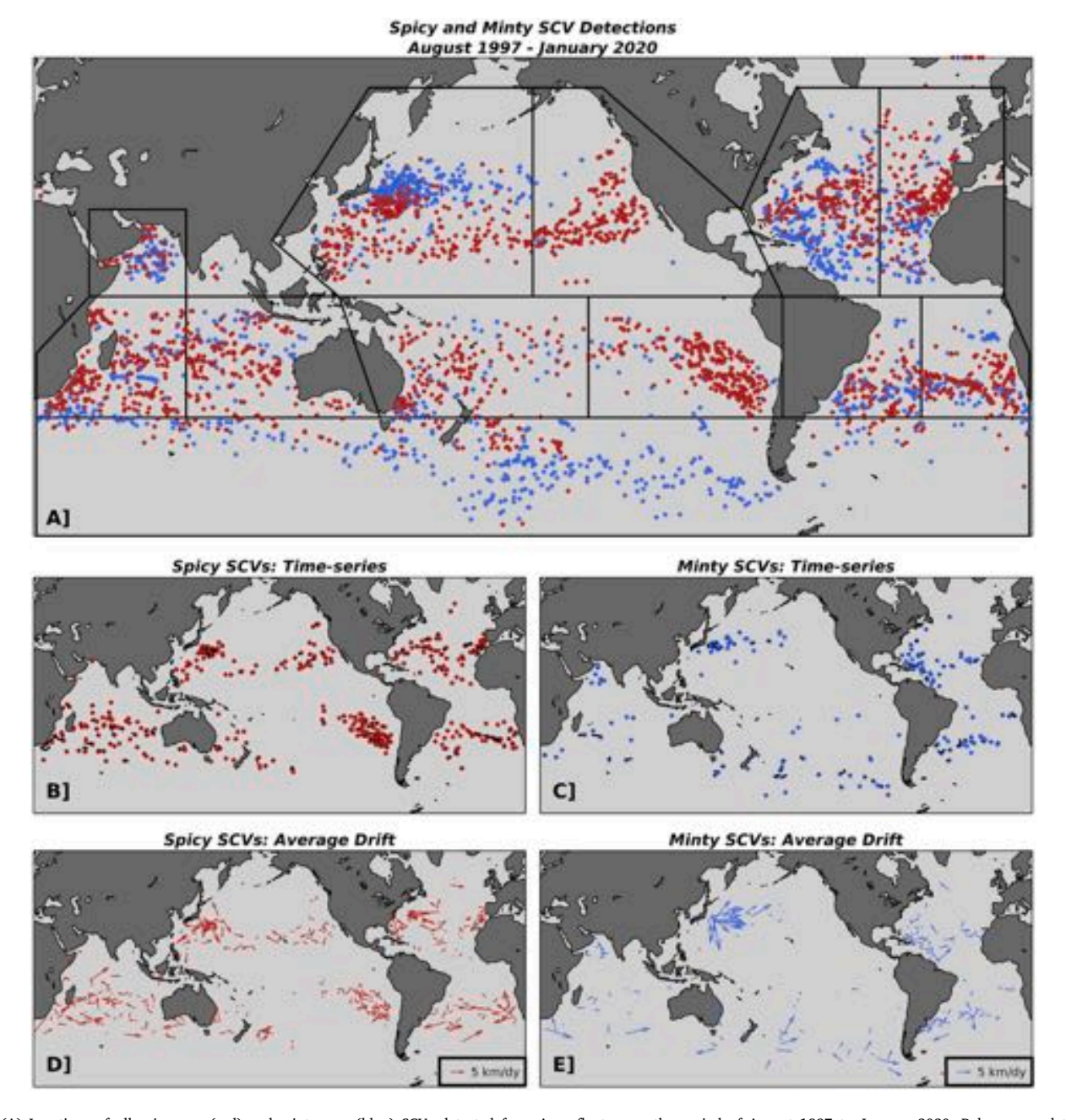


Fig. 4. (A) Locations of all spicy-core (red) and minty-core (blue) SCVs detected from Argo floats over the period of August 1997 to January 2020. Polygons used to group SCV statistics for regional analyses (Figs. 7–9) are shown in black. (B,C) Initial locations of spicy-core and minty-core SCV time-series, shown as red and blue dots respectively, from repeatedly sampled SCVs measured from consecutive Argo float casts. Time-series trajectories are shown as thin black lines. (D,E) Average drift speed and direction (shown as vector arrows) calculated from each spicy-core and minty-core SCV time-series, respectively. (For interpretation of the references to color in this figure legend, the reader is referred to the web version of this article.)

chain, with sparser detections throughout the western end of the low-latitude subtropical gyre. Distributions of core hydrographic properties (Fig. 7) and their respective scatter maps (Fig. 5) suggest that at least two overlapping populations exist. Most are found along the western boundary between 26.5–27.2 kg m $^{-3}$, with core temperatures and salinities between 5–10 °C and 34.2–35 PSU respectively; a smaller number of SCVs, mostly within the subtropical gyre, contain cores at 25.8–26.2 kg m $^{-3}$, with core temperatures of 10–16 °C.

Within the same region, we also identify 274 minty-core SCVs concentrated in the Kuroshio extension at slightly higher latitudes and over a larger geographical area than the co-located spicy-core SCVs (Fig. 6). In general, the cores of these minty SCVs are found on the same isopycnal range as the larger population of spicy-core SCVs, but with slightly decreased temperature and salinity values. Additionally, the

minty-core SCVs show a trend of decreasing temperature and spiciness with latitude (Fig. 6A and C). Core pressure and vertical thickness distributions are very similar across spicy and minty-core SCVs, suggesting that the majority propagate at 300–800 dbar, with thicknesses of 500 m or less. A relatively large number of SCV time-series are observed to the east of Japan, with no obvious preference for drift direction, identifying this region as a potential source of long-lived SCVs throughout the Northwest Pacific (Fig. 4B–E).

In contrast to the northwest populations, the Northeast Pacific is largely characterized by predominately spicy-core SCVs (160 detections versus 10 minty-core) that appear to be one coherent population based on both property distributions and scatter maps (Figs. 5 and 7). Histograms show relatively small spread and indicate that their typical core temperature and salinity range from 6–12 °C and 34.1–34.6 PSU,

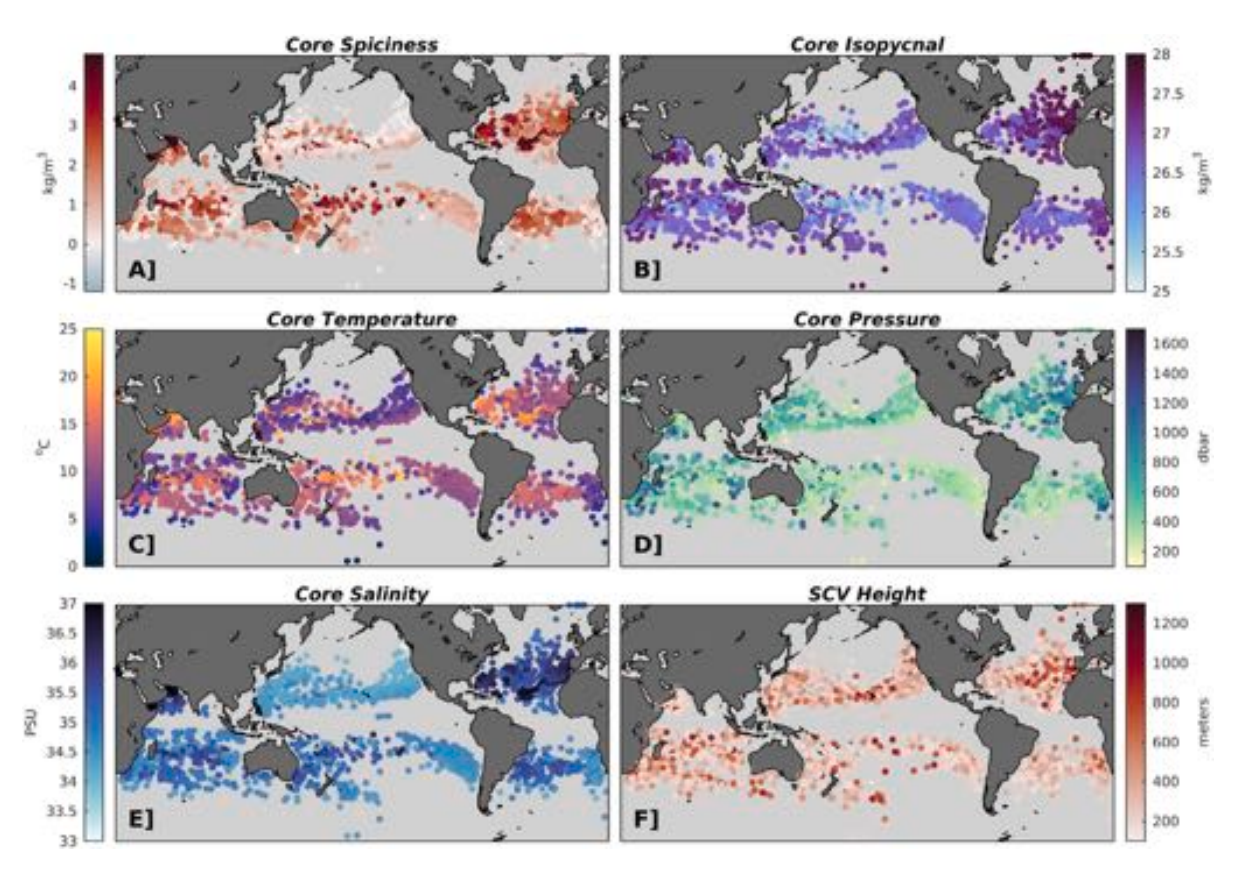


Fig. 5. Spicy-core SCV detection locations, colored by (A) core absolute spiciness, (B) core isopycnal, (C) core temperature, (D) core pressure, (E) core salinity, and (F) SCV vertical thickness.

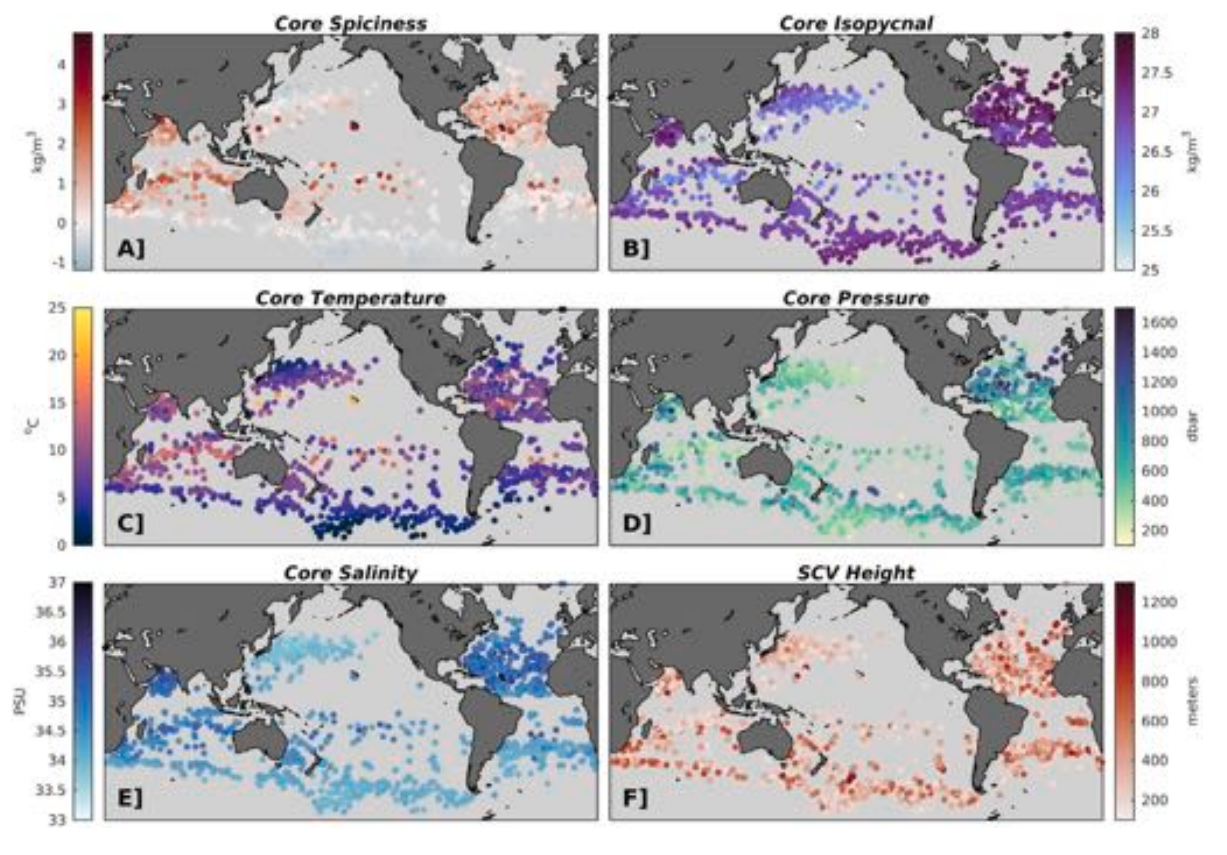


Fig. 6. Same as Fig. 5, but for minty-core SCV detections.

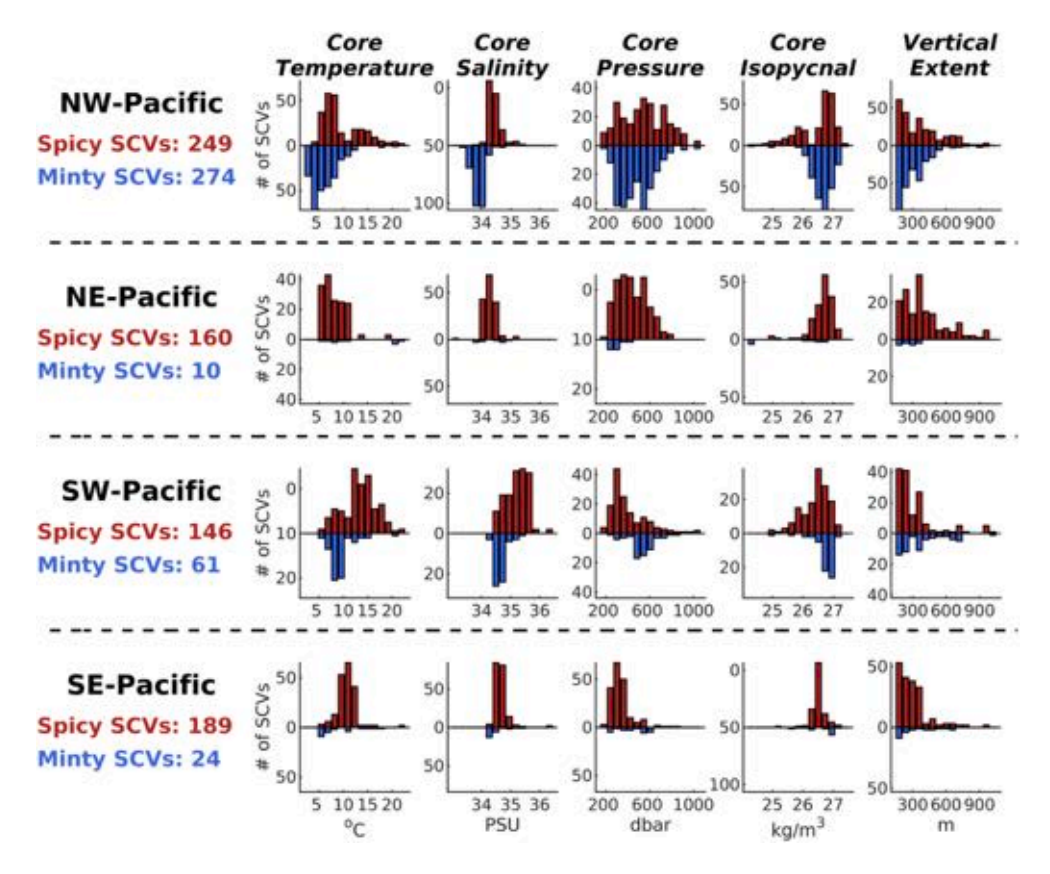


Fig. 7. Histograms of SCV core temperature, core salinity, core pressure, core isopycnal, and vertical thickness from the northwest, northeast, southwest, and southeast Pacific regions (respectively). Regions are outlined in Fig. 4. Red bars show spicy-core SCV distributions, and blue bars minty-core SCVs. (For interpretation of the references to color in this figure legend, the reader is referred to the web version of this article.)

respectively. Most are found propagating at core pressures and isopycnals of 250–700 dbar and 26.2–26.8 kg m⁻³ respectively, with typical vertical thickness of 250–500 m. Spatially, they are distributed along the eastern boundary from the Baja California Peninsula to Vancouver Island, extending out to the Hawaiian Islands. This pattern can be explained by drift observations from the numerous SCV time-series within the region, as evidenced by panels B and D in Fig. 4, which collectively indicate southwestward propagation from the eastern boundary into the subtropical gyre. Similar to the minty-core population in the Northwest Pacific, SCV property maps in Fig. 5 indicate that SCV cores become slightly less warm and salty and propagate along denser isopycnals as they are detected more poleward.

SCV spatial distributions within the South Pacific largely mirror those from the North Pacific; both spicy-core and minty-core SCVs are detected in the western end of the basin, whereas spicy-core SCVs dominate detections in the east. Minty-core SCVs in the Southwest Pacific (61 detections) are mostly observed between Australia and New Zealand and show uni-modal distributions across many properties. Typical SCVs exhibit core temperatures of 5-10 °C, salinity values of 34.1-34.7 PSU, and propagate along core isopycnals between 26.9-27.1 kg m⁻³ at depths of 500-700 dbar (Fig. 7). However, despite consistent properties across detections in this region, there is a notable lack of SCV time-series, suggesting that these may be relatively short-lived features. Spicy-core SCVs (146 detections) are also prevalent east of Australia, notably with more time-series observations, but at slightly lower latitudes and with additional scattered observations spread throughout the western end of the subtropical gyre. Compared to the minty-core detections, spicy-core SCVs show a much wider range of SCV core values with several peaks; however, mapped properties in Fig. 5 show ~3 distinct populations occupying waters to the west, north, and southeast of New Zealand.

The Southeast Pacific shares remarkably similar population characteristics with the Northeast Pacific spicy-core detections, albeit with less spread. Distributions from the 189 spicy-core detections in the region show SCVs with core temperatures and salinity values between 8-12 °C and 34.1-34.8 PSU, respectively, which propagate along a small range of isopycnals (26.2-26.8 kg m⁻³). They are concentrated along the coast of Chile and extend into the subtropics, as indicated by the spatial extent of detections and the numerous SCV time-series showing predominantly northwestern propagation (Fig. 4). As for the Northeast Pacific SCVs, detections exhibit a pattern of SCV cores becoming slightly cooler and fresher as they are observed more poleward. The similar distributions and spatial patterns of both the northeastern and southeastern spicy-core detections in the Pacific suggests that a common generation mechanism consistently produces spicy-core SCVs along the eastern boundary of the Pacific, which are capable of reaching the interiors of the subtropical gyres.

3.2. Atlantic SCVs

The North Atlantic exhibits more spatial variability in detections when compared to the other basins, possibly because of the relatively smaller basin width; however several notable patterns emerge. Of the 163 spicy-core SCVs identified throughout the Northwest Atlantic, a population of relatively warm (15–20 °C) and salty (36.0–36.3 PSU) SCVs is observed extending northeast from the Florida coastline into the central North Atlantic along the ~ 26.5 isopycnal, at depths of roughly 300–700 dbar (shown clearly by the high spiciness values in Fig. 5A). In the Eastern North Atlantic, where we identify 152 spicy-core SCVs, a population of SCVs with slightly colder core temperatures (10–15 °C) propagating along denser isopycnals ($\sim 27.5~{\rm kg~m}^{-3}$) appears to originate along the eastern boundary near the Iberian peninsula, overlapping with the western population

throughout the central Atlantic (Fig. 8). SCV time-series detections (Fig. 4) further indicate that these distributions belong to two separate populations, which emanate from the Gulf Stream region in the western Atlantic and the Mediterranean outflow in the east, and eventually overlap in the central Atlantic, albeit at different depths. Finally, the low-latitude North Atlantic also includes a separate smaller, coherent population of spicy-core SCVs. Time-series from this population indicate that they propagate westward, which, coupled with their spatial property distributions in Fig. 5, suggests a source near the Canary Islands.

Minty-core SCVs in the Northwest Atlantic (212 detections) are heavily concentrated along the western boundary, from the northeastern coast of Brazil to Nova Scotia, whereas the 86 detections in the Northeast Atlantic are largely found in two clusters centered near the Canary Islands and off the coast of Mauritania. Distributions of core properties for both sub-basins show significant spread across all properties, yet indicate that most minty-core SCVs propagate along isopycnals ranging from 27.0-28.0 kg m⁻³, with core salinity values of 34.5-35.5 PSU (Fig. 8). The Western North Atlantic, however, exhibits peaks at slightly colder core temperatures (~ 4-6 °C versus 7-9 °C), and at the 27.0-27.2 kg m⁻³ isopycnal range (versus a more even distribution in the east). SCV property maps in Fig. 6 show less coherent spatial patterns in the Western North Atlantic than in the east, where in general the SCVs near the Canary Islands exhibit slightly saltier cores than the Mauritania population to the south. SCV time-series are found all throughout the western population of minty-core SCVs, whereas they are only detected within the Canary population in the east (Fig. 4).

The South Atlantic basin is largely defined by a zonal band at roughly 30°S of both spicy and minty-core SCVs, extending between Namibia and the southernmost extent of Brazil (Figs. 5 and 6), with westward propagating SCV of both types (Fig. 4). The 83 spicy-core SCVs throughout the Southwest Atlantic show uni-modal property distributions, with SCVs generally propagating at ~ 400 dbar along the 26.5 kg m⁻³ isopycnal, while exhibiting core temperature and salinity values ranging between 12-16 °C and 35-36 PSU respectively (Fig. 8). Minty-core SCVs in both the West (55 detections) and the East (63) South Atlantic have remarkably similar properties, suggesting one coherent population propagating at roughly 600-800 dbar along the \sim 27.0 kg m⁻³ isopycnal, with core temperatures of roughly 4-6 °C, and salinity values between 34.0-34.5 PSU. In contrast, the Southeast Atlantic spicy-core SCV distributions (106 detections) are bi-modal, but show similar peaks in core temperature, salinity, pressure, and isopycnal as in the western spicy-core SCVs. The secondary peak across property distributions results from a separate population of deeper (~ 800 dbar versus ~ 400 dbar) spicy-core SCVs with relatively colder (5-10 °C) and fresher (34.0-34.5 PSU) cores that are zonally distributed along the eastern boundary between South Africa and Angola (seen clearly in Fig. 5A). This population also exhibits the pattern observed in the spicy detections within the eastern regions of the Pacific and North Atlantic, where SCV spiciness decreases poleward.

3.3. Indian SCVs

SCV detections within the North Indian Ocean are concentrated within the Arabian Sea, where we found 40 spicy-core and 64 minty-core detections. Spicy-core SCVs with relatively warm and salty cores (~ 17 °C and >37 PSU) are detected near the Gulf of Oman and the Red Sea outflow regions. However, detections in the offshore region to the east show more heterogeneous properties, as evidenced by the spread in histograms from Fig. 9. Notably, the only spicy-core SCV time-series detected in this region are confined to the outflow regions (Fig. 4). Minty-core SCVs are mostly found overlapping with the offshore spicy-core SCVs in the central Arabian Sea, where they also exhibit significant spread across core properties, albeit with significantly more numerous time-series detections as evidenced by Fig. 4. While both spicy and

minty SCV core pressures show a wide range, nearly all SCVs exhibit vertical thickness of less than 400 m.

In the Southern Indian Ocean, we detect 313 spicy-core SCVs mostly distributed along zonal bands with contrasting core properties between Madagascar and Australia (Fig. 5). The center of the basin between 20-25°S exhibits SCVs with relatively high values of temperature and salinity compared to the zonal bands at lower and higher latitudes. SCV time-series are prevalent throughout the region and generally show westward propagation, with slightly more observations in the central zonal band. This result, coupled with the similarities in distributions across both eastern and western spicy-core SCVs (Fig. 9), suggests a connection across the basin between the two populations. Minty-core SCVs (133 detections) are similarly identified at the same low and high latitudes as spicy-core SCVs, but in contrast are largely absent throughout the 20-25°S band. Despite large spread in core distributions (Fig. 9), SCV property maps in Fig. 6 again show similarities across zonal sections. Finally, the southeast coast of South Africa and to a lesser extent the waters off of Tanzania are additional zones of spicy and minty-core SCV observations. However, property maps suggest high variability in their characteristics, despite several prevalent spicy-core time-series detections.

3.4. Southern ocean SCVs

Minty-core SCVs with coherent properties are identified along a high-latitude band throughout the Southern Ocean (defined here as poleward of 40°S). Distributions (Fig. 9) and SCV property maps (Fig. 6) show remarkable consistency across detections, with a notable pattern of slightly greater core temperature ($\sim 5-8$ °C versus $\sim 0-5$ °C) within the high latitude Indian Ocean compared to the Pacific. Nearly all detected SCVs propagate at core pressures of 300–800 dbar along core isopycnals ranging from 26.9–27.5 kg m $^{-3}$, which, coupled with similarities in core temperature and salinity, suggest a common formation mechanisms throughout the Southern Ocean in the vicinity of the ACC. Given their proximity to the minty-core detections, spicycore SCVs identified at high latitudes throughout the South Indian basin and to the southeast of New Zealand in the Pacific may also have a generation source associated with the ACC.

4. Discussion

Global and regional maps of SCV properties (Figs. 5 through 9) reveal several notable SCV populations with coherent properties, such as the wide-spread spicy SCVs along the eastern boundary of the Pacific Ocean and the zonal band of minty SCVs throughout the Southern Ocean. These results strongly suggests generation of SCVs with similar hydrographic features in those regions. However, in order to estimate the regional frequency of SCV generation, we need to account for the uneven spatial sampling density of Argo. Notable locations such as the Kuroshio extension have a much higher number of Argo casts within the record than the Southern Ocean, for example, as observed after binning Argo casts into $4^{\circ} \times 4^{\circ}$ latitude/longitude cells (Fig. 10A). After accounting for this discrepancy in sampling density, we estimate the SCV frequency by binning detections within the same grid, as shown in panels B-D of Fig. 10. This provides a metric to identify zones with relatively high frequency of SCV observations that are also characterized by consistent SCV properties.

Figs. 4 and 10 reveal several remarkable hot-spots that exhibit the presence of SCV time-series, a higher spatial density of detections, and relatively coherent SCV-core properties. Notably, these criteria are common in close proximity to: (1) major eastern boundary upwelling systems (EBUS); (2) outflow from marginal seas such as the Mediterranean and Red Seas; (3) large oceanic fronts such as the ACC and those associated with western boundary current separation. The following sections explore possible generation mechanisms associated with these regions. To do so, we gather populations of SCVs near these oceanic

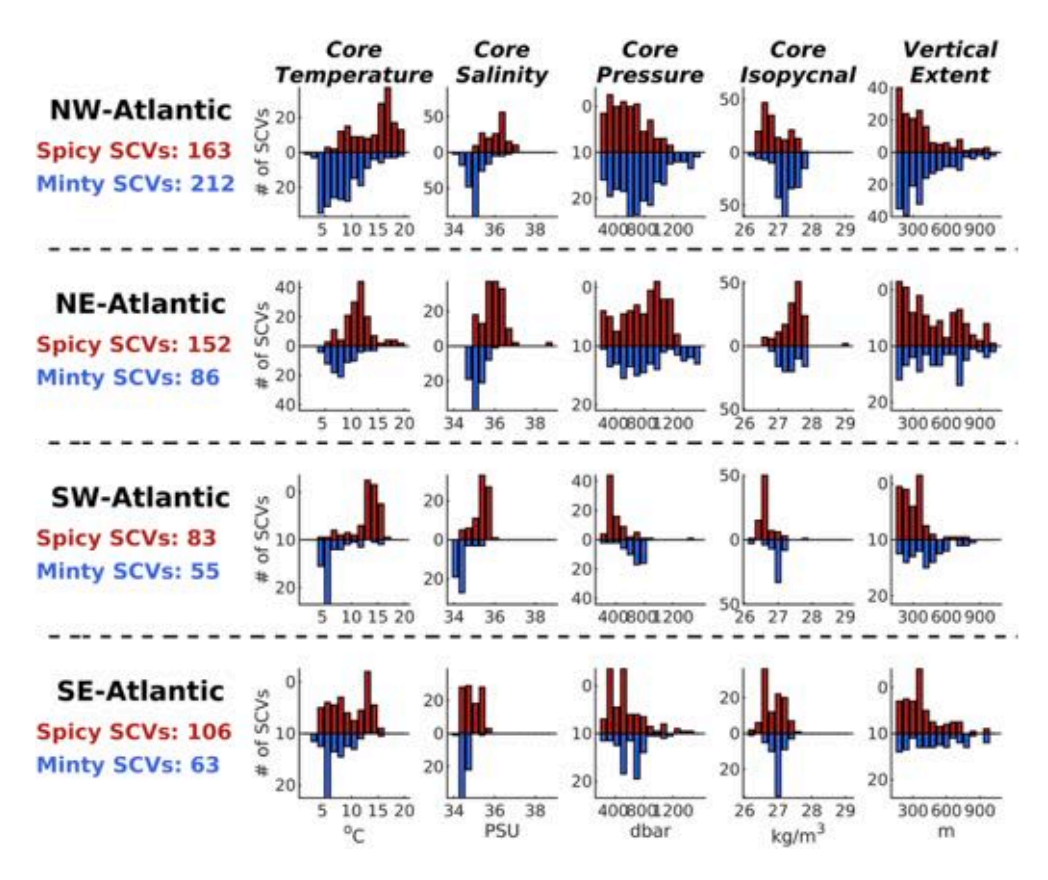


Fig. 8. Same as Fig. 7, but for the northwest, northeast, southwest, and southeast Atlantic regions (respectively). (For interpretation of the references to color in this figure legend, the reader is referred to the web version of this article.)

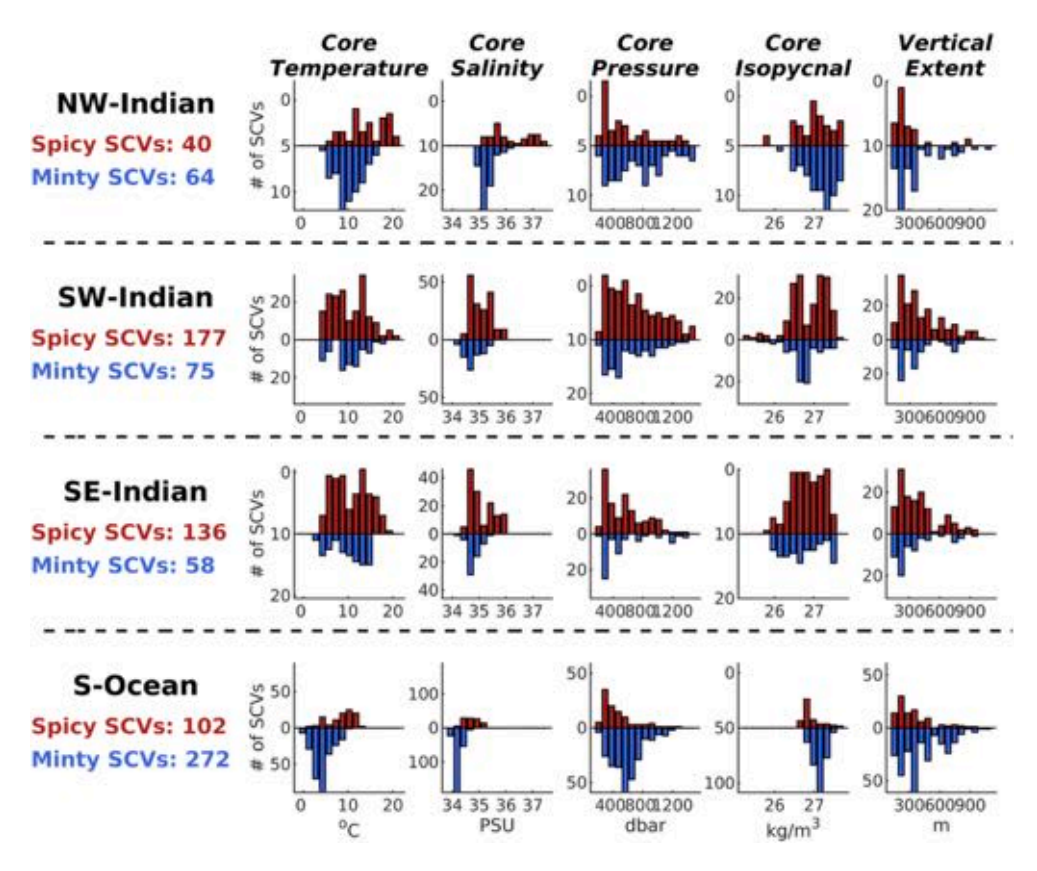


Fig. 9. Same as Fig. 7, but for the northwest, southwest, and southeast Indian and Southern Ocean regions (respectively). (For interpretation of the references to color in this figure legend, the reader is referred to the web version of this article.)

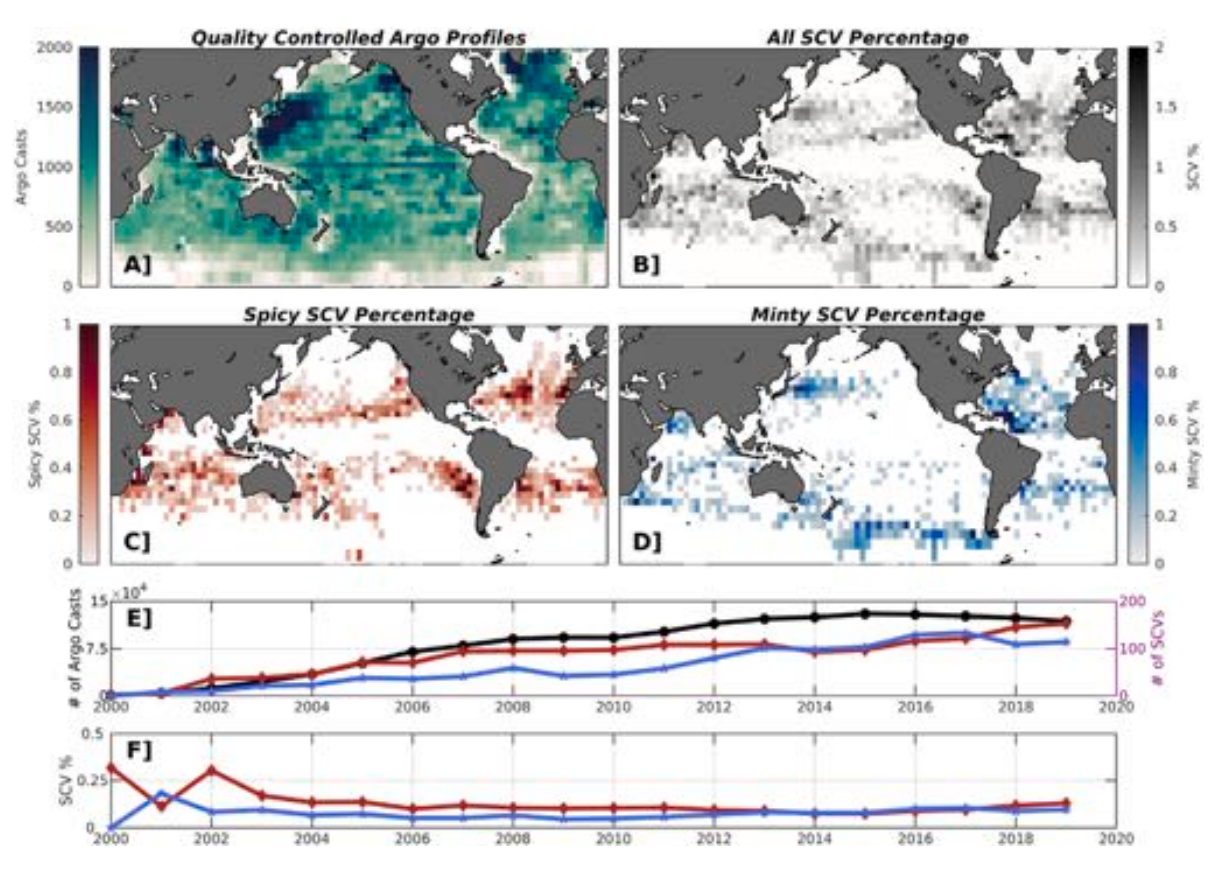


Fig. 10. (A) Number of quality controlled Argo profiles within 4° × 4° longitude/latitude grid boxes. (B) Percentage of unique SCV detections. Panels C and D show the gridded percentages from spicy-core and minty-core detections (respectively). (E) Time-series of the total number of quality controlled Argo casts (black line, left y-axis) and the total number of unique spicy-core and minty-core detections (red and blue lines, right y-axis). (F) Annual SCV percentage of spicy-core (red) and minty-core (blue) SCVs. (For interpretation of the references to color in this figure legend, the reader is referred to the web version of this article.)

features and connect their characteristics with regionally persistent currents and water masses. When necessary, to characterize hydrographic profiles of water masses, we identify approximate temperature and salinity curves by averaging Argo profiles near their geographic source regions using 5° latitude/longitude cells. We also highlight persistent fronts using a mean sea surface dynamic topography derived from jointly analyzed data of drifters, satellite altimetry, wind, and gravity for the decade 1992–2012 (retrieved online from http://apdrc.soest.hawaii.edu/datadoc/mdot.php). Fronts associated with the ACC are demonstrated using results from the WOCE Southern Ocean Atlas (Orsi and Whitworth, 2005).

4.1. Poleward flow along eastern boundaries

The four major EBUS in the Pacific and Atlantic are the California, Peru-Humboldt, Canary, and Benguela upwelling systems. These regions are found along the eastern flanks of their respective subtropical gyres, driven by persistent equatorward winds along their meridional coastlines (Bakun and Nelson, 1991). The resulting equatorward currents in each EBUS (the California Current, the Peru-Humboldt Current, the Canary Current, and the Benguela Current, respectively) carry high-latitude waters, whereas characteristic undercurrents flowing at mid-depths over the shelf and slope (Chavez and Messié, 2009) carry subsurface equatorial waters poleward. The global SCV detections highlight each EBUS as sites of frequent long-lived SCV generation, as evidenced by Figs. 4 and 10; thus the unique wind-forced dynamics of these systems appear to promote SCV generation.

Model simulations of eastern boundary undercurrents (Molemaker et al., 2015) have shown that they develop anticyclonic vertical vorticity along their poleward path due to the effect of bottom drag against the continental slope. Separation from the slope near ridges or areas

of strong topographic curvature causes offshore diversion, followed by centrifugal and submesoscale instabilities, vigorous mixing, and organization of the flow into anticyclonic vortices (Dewar et al., 2015; Molemaker et al., 2015; Southwick et al., 2016). To explore the role of these undercurrents in the generation of SCVs detected near EBUS, we compare the temperature and salinity of equatorial surface currents and poleward undercurrents with similar T–S curves from SCV detections.

In the North Pacific, the California Current advects relatively cold, fresh and oxygen-rich Pacific Subarctic Upper Water (PSUW) equatorward from roughly 45 ° N (Lynn and Simpson, 1987; Thomson and Krassovski, 2010), whereas the poleward California Undercurrent transports relatively warm, salty and oxygen-poor Pacific Equatorial Water (PEW) as far North as the Aleutian Islands (Thomson and Krassovski, 2010). Panel A in Fig. 11 provides details from a subset of SCVs detected off of the California upwelling system. Spicy-core SCVs are detected from the Baja California Peninsula to as far as Vancouver Island, with spatial distributions and SCV time-series suggesting southwestward propagation towards the Hawaiian Islands, consistent with β-plane drift westward and equatorward (Cushman-Roisin and Beckers, 2011). A representative profile off of Baja California (star marker in Fig. 11A) reveals a typical peak in salinity centered just below the salinity minimum at 200 dbar, surrounded by anomalously high temperatures throughout the SCV extent. These characteristics, along with the uni-modal distribution of core isopycnal centered at roughly 26.6 kg m⁻³, match descriptions of 'Cuddies' from the literature, likely generated from the California Undercurrent via the processes outlined above (Simpson and Lynn, 1990; Chaigneau et al., 2011; Pelland et al., 2013; Collins et al., 2013; Garfield et al., 1999; Li et al., 2017; Steinberg et al., 2018). Indeed, T-S diagrams of detected SCVs versus curves of PEW (dashed black curve in Fig. 11A) and PSUW (solid black curve)

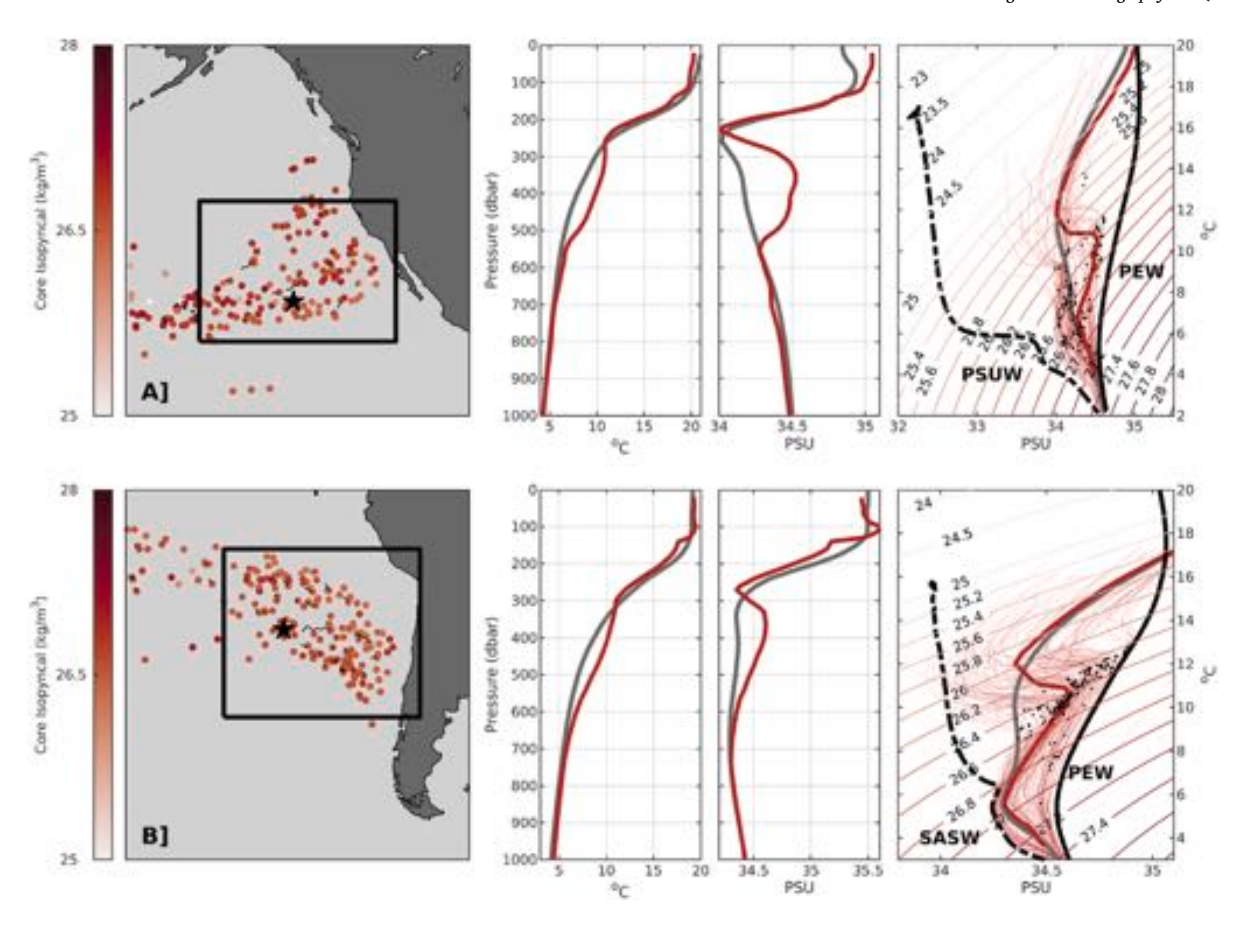


Fig. 11. (A) Locations, colored by core isopycnal, and hydrographic properties of spicy-core SCVs detected near the California upwelling system. Thin black lines indicate propagation of SCVs with multiple casts. Temperature and salinity profiles and diagrams are constructed from the star marker profile (Argo float 4900691, cycle 85, solid red curve), with the gray curve representing the climatological profile for that cast's location and month. T–S curves for all other detections with the boxed region are shown as thin red lines, with black dots representing core temperature and salinity values. (B) Same as (A), but for the spicy-core SCVs off of the Peru-Humboldt upwelling system, with the example profile from Argo float 3900328 cycle 141. Approximate curves of Pacific Equatorial Water (PEW, both panels), Pacific Subarctic Upper Water (PSUW, panel A) and Subantarctic Surface Water (SASW, panel B) are also shown. (For interpretation of the references to color in this figure legend, the reader is referred to the web version of this article.)

show a high influence of PEW in their cores, despite many being detected well offshore of the coastline.

Equatorward offshore flow in the South Pacific is dominated by the Peru-Humboldt Current, which transports relatively cold and fresh Subantarctic Surface Water (SASW) from the north of the Subantarctic Front along the coasts of Chile and Peru (Schneider et al., 2003). Countering the surface flow is the Peru-Chile Undercurrent, of similar origin to the California Undercurrent, wherein PEW water flows from the equator southward along the continental slope of South America (Johnson and McTaggart, 2010). Panel B in Fig. 11 outlines a subset of spicy-core SCVs detected off of the Peru-Humboldt upwelling system. A representative SCV from the region (star marker in 11B) reveals typical SCV cores below the halocline, with pronounced salinity maxima at roughly 300-500 dbar, and anomalously warm temperatures down to 600 dbar or deeper. A relatively large number of SCVs in this region are sampled multiple times by the same floats (thin black lines) and show northwestward propagation, consistent with β -plane drift. Descriptions of anticyclonic eddies in this region (Johnson and McTaggart, 2010; Chaigneau et al., 2011; Colas et al., 2012; Hormazabal et al., 2013; Combes et al., 2015) attribute formation to the same undercurrent processes outlined above for Cuddies, leading to spicy-core SCVs. Similar to the North Pacific population, T-S diagrams suggest that SCVs in this region contain a high percentage of PEW versus SASW, placing their origin within the undercurrent.

The Canary Current system extends from the coast of Morocco to Cape Blanc, Mauritania and is distinct from the other EBUS due to opposite hydrographic characteristics. The equatorward current advects

relatively warm and salty North Atlantic Central Water (NACW) equatorward, whereas relatively cooler, fresher, and nutrient-rich South Atlantic Central Water (SACW) is advected poleward at the surface by the Mauritania Current (Kämpf and Chapman, 2016), and similarly to the south of Cape Blanc by a poleward undercurrent along the shelf break (Schütte et al., 2016; Klenz et al., 2018). Panel A in Fig. 12 shows the Mauritania detections, which in contrast to other EBUS are characterized by predominately minty-core SCVs. From the limited observations, histograms suggest that most minty-core SCVs off of Mauritania propagate between 400-800 dbar along the 26.9 -27.4 isopycnal surfaces, with typical core temperatures and salinities ranging between 6-10 °C and 34.8-35.2 PSU respectively. Profiles from the region (see star marker example in Fig. 12A) reveal that most cores are positioned well below the base of the shallow pycnocline, where they appear as a homogeneous layer of relatively cold and fresh water that often represents the salinity minimum. The T-S diagram for the population clearly shows an influence of SACW in their cores, which is relatively cold and fresh in the North Atlantic (hence, the minty-core populations). Several other studies have reported on similar subsurface eddies with cores of anomalously low temperature and salinity in the Mauritania region, often described as "dead zone" anticyclonic mode water eddies (ACME) because of the low oxygen concentration (Karstensen et al., 2015; Schütte et al., 2016; Grundle et al., 2017; Thomsen et al., 2019; Hauss et al., 2016), with several found to last up to 200 days (Karstensen et al., 2017). Thus, while further observations are still needed, the above results suggest SCVs generation in this region via undercurrent instabilities, likely at prominent topographic

features (Schütte et al., 2016), which encapsulate volumes of SACW before advection westward into the subtropical gyre.

The Benguela upwelling system along the west coast of Africa in the South Atlantic is driven by the equatorward Benguela Current, which carries cold Eastern South Atlantic Central Water (ESACW) from Africa's southern tip to roughly 15-16 ° S. At its northernmost extent, the Benguela Current meets the poleward Angola Current, which transports relatively warmer and saltier SACW (as opposed to the colder and fresher counterparts in the North Atlantic) to form the Angola-Benguela front zone (Lass and Mohrholz, 2008). The Angola current periodically (typically September to November and February to April) breaks through the front to continue poleward as the Benguela Undercurrent along the shelf (Lass et al., 2000; Mohrholz et al., 2001), supplying subsurface SACW to the northern Benguela system (Siegfried et al., 2019). Panel B in Fig. 12 describes the spicy-core SCVs detected off of Namibia, which show generally similar distributions in core properties to the Mauritania minty-core SCVs. An example profile for the region shows a core of relatively warm and salty water at roughly the same depth as the example shown for Mauritania. Similar to the North Atlantic minty-core SCVs off of Mauritania, T-S diagrams suggest that Benguela spicy-core SCVs contain higher percentages of SACW, indicative of an origin within the Benguela Undercurrent, Pegliasco et al. (2015) documented subsurface anticyclonic eddies originating from the Benguela Current, while model simulations from Frenger et al. (2018) also suggested that similar, low-oxygen eddies in the region are generated via undercurrent instabilities. T-S signatures of the SCVs generated within that study largely agree with our Benguela detections, providing more evidence of an origin within the undercurrent.

In summary, our results highlight the eastern boundary of the Pacific Ocean as significant sources of long-lived and far-reaching SCVs. This conclusion mirrors those of several previous studies (Johnson and McTaggart, 2010; Pelland et al., 2013; Frenger et al., 2018), which suggest that these SCVs could modify the mean properties of the Pacific subtropical gyres by introducing warm, salty, and oxygen-poor/nutrient-rich PEW waters. A similar mechanism may also occur in the Atlantic, via westward propagation of SACW waters, but on a smaller scale given the large disparity in detections. Regardless, SCVs generated from these systems may alter the characteristics of both local and adjacent water masses by exporting poleward undercurrent signatures away from EBUS, while also contributing to subtropical gyre tracer budgets (Frenger et al., 2018).

4.2. Marginal sea overflow

Dense water outflows originating from marginal seas and continental shelves are major components of the Earth climate system, given their contributions to intermediate and deep water masses of the world's oceans (Warren and Wunsch, 1981; Vic et al., 2015). After flowing into the open ocean, instability processes govern the dispersal of overflow waters, which can take place over hundreds or thousands of kilometers depending on the basin dynamics (Legg et al., 2009; Vic et al., 2015). For example, overflow from the Mediterranean encounters a region with relatively low background eddy activity, allowing for a gravity current which, after achieving neutral buoyancy, is deflected to form a boundary-intensified poleward flow (Bower et al., 1997; Legg et al., 2009) similar to an EBUS undercurrent. Other notable outflows, such as the Persian Gulf outflow near the Gulf of Oman and the spread of Red Sea Water in the Gulf of Aden, equilibrate at shallower depths and encounter vigorous mesoscale variability which actively participates in spreading the dense plumes (Vic et al., 2015; Morvan et al., 2019). Given their ability to transport water mass volumes over significant distances, SCVs could play a role in spreading these overflow waters away from the formation regions.

Perhaps the most notable and well studied examples are the Mediterranean outflow eddies ('Meddies'). Large segments of the boundary-intensified overflow jet have been shown to separate near

the southwestern tip of the Iberian peninsula in the form of warm, salty Mediterranean Water lenses of roughly 20 km diameter (Bower et al., 1997; Richardson et al., 2000; McWilliams, 2019), with one or two vertically aligned cores typically centered between 800 and 1200 m (Bashmachnikov et al., 2015). Those that avoid collision can last for several (4–5) years, propagating as far as the mid-Atlantic ridge (Richardson et al., 2000; Ménesguen et al., 2012; Barbosa Aguiar et al., 2013) before dissipation by double-diffusive mixing (Radko and Sisti, 2017). With estimates suggesting that they support about 50% of the westward salt flux from the Mediterranean (McWilliams, 1985; Bower et al., 1997), these SCVs have a far-reaching impact on the tracer budget of the North Atlantic, in addition to their contribution to the Mediterranean salt tongue, one of the prominent hydrographic features of the mid-depth North Atlantic (Richardson et al., 2000).

Panel A in Fig. 13 outlines a subset of spicy-core SCVs identified near the Mediterranean outflow. Temperature and salinity profiles from the population are in good agreement with previous descriptions of Meddies, showing large temperature (~ 4 °C) and salinity (~ 1 PSU) anomalies centered at roughly 1000 dbar. As reported in other studies, a large number contain two cores at roughly 800 and 1200 dbar and are sampled over consecutive Argo cycles for many months (see Fig. 3 for a notable example). The adjacent region next to the Mediterranean outflow also exhibits some of the highest frequency in SCV detection across the ocean ($\sim 1\%$ of all Argo casts in that region, Fig. 10), with panel D in Fig. 4 suggesting that many are long lasting. Together, these results support the role of Meddies in modulating the heat and salt budget of the North Atlantic by periodically advecting volumes of Mediterranean water, often over several thousand kilometers.

The Arabian Sea is also influenced by two separate outflows originating in the Persian Gulf and the Red Sea, which settle at 250-300 m and 600-1000 m depths into the Gulf of Oman and into the Gulf of Aden, respectively (Morvan et al., 2019). In contrast to the Gulf of Cadiz with Mediterranean outflow water, the Arabian Sea is home to a relatively energetic mesoscale eddy field that provides a different dynamical regime for the spreading of outflow waters (Bower and Furey, 2012; Carton et al., 2012; Morvan et al., 2019; Vic et al., 2015). Mesoscale surface eddies have been shown in modeling studies and in-situ observations to divert the outflow paths away from the coast, advecting them instead along curved trajectories corresponding to the local eddy vorticity (Carton et al., 2012). As these eddies approach the coast, frictional effects due to the slanted bottom boundary layer generate opposite-signed relative vorticity on the slope in the form of elongated filaments of outflow waters. Strong lateral shear leads to instabilities that break apart these filaments into submesoscale vortices with cores of outflow water, which then propagate away from their region of formation if paired with a surface eddy (Molemaker et al., 2015; Morvan et al., 2019; Vic et al., 2015).

Panel B in Fig. 13 shows a collection of detections identified near the Gulf of Oman. Profiles indeed show anomalous cores of hot and salty water at roughly 200–300 dbar, indicative of Persian Gulf overflow waters, and compare well with previously reported anticyclonic lenses observed in this region (L'Hégaret et al., 2016). However, as noted by Bower and Furey (2012) and L'Hégaret et al. (2016), SCVs at these outflows are generally short-lived due to their generation along western boundaries, where strong horizontal shear by mesoscale eddies and westward self-propagation back towards the source region may lead to rapid destruction.

As shown in previous studies, the generation of SCVs at major outflows plays a non-negligible role in transport and dispersion of these regionally important water masses. The same mechanism responsible for producing SCVs at EBUS (subsurface boundary current separation) generates Meddies, while SCVs generated within the Arabian Sea outflows appear to be more ephemeral due to their formation within more energetic western boundary systems. This further highlights the importance of dynamical differences along eastern versus western ocean boundaries. In more quiescent environments found near eastern boundaries, SCVs are capable of transporting origin water masses over great distances, whereas vigorous mesoscale activity along western boundaries may confine their regional reach.

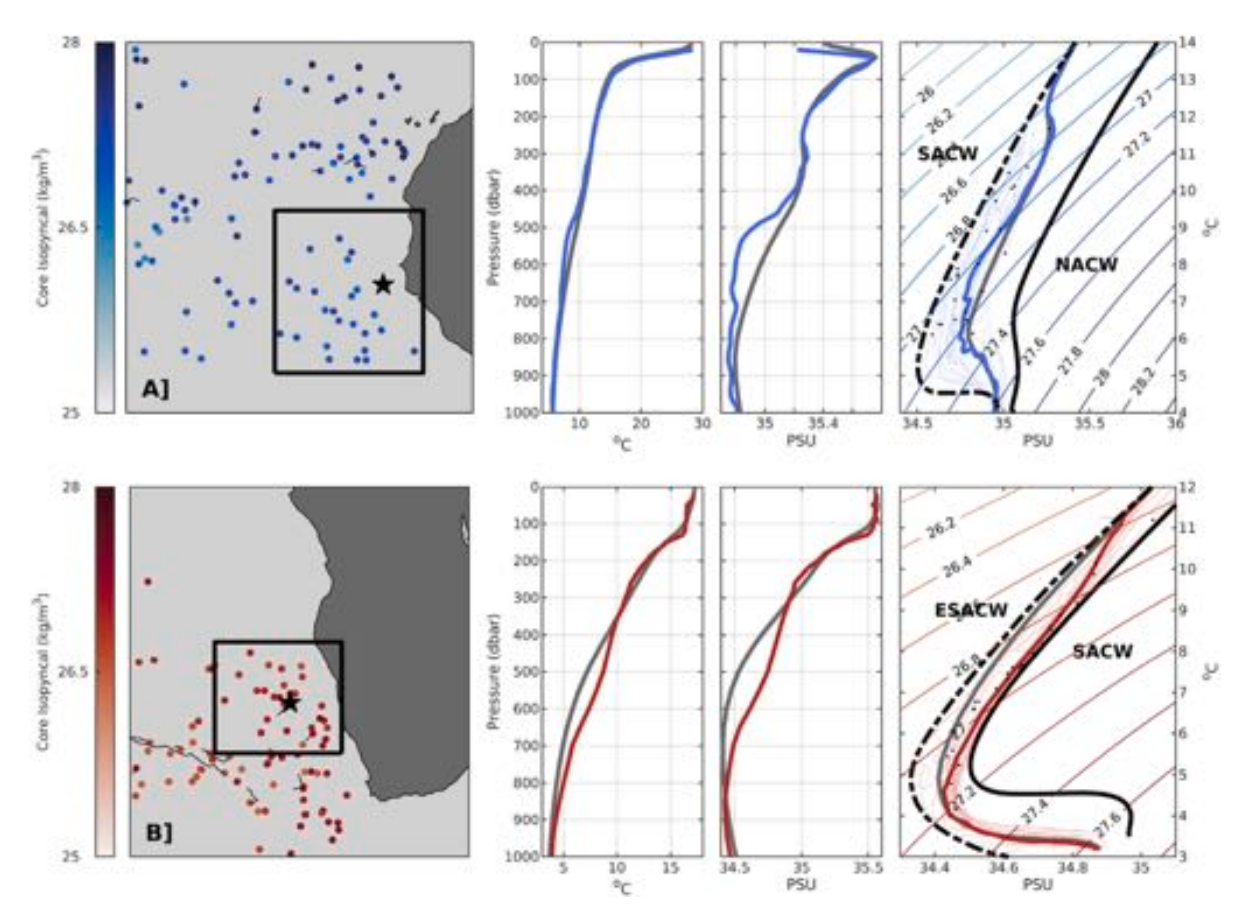


Fig. 12. (A) Same as panel A in Fig. 11, but for the minty-core SCVs detected off of the Mauritania coastline. The example profile is from Argo float 6900919 cycle 130. (B) Same as (A), but for the spicy-core SCVs detected off of the Benguela upwelling system, with the example profile from Argo float 1901238 cycle 38. Approximate curves of South Atlantic Central Water (SACW, both panels), North Atlantic Central Water (NACW, panel A) and Eastern South Atlantic Central Water (ESACW, panel B) are also shown.

4.3. Mode water eddies

As revealed by Figs. 4 and 10, frequent and long-lived SCVs occur within regions of mode water formation. Mode waters originate from deep mixed layers caused by winter convection (Hanawa and Talley, 2001; Xu et al., 2016), occurring in conjunction with persistent fronts that often separate these homogeneous water masses from more stratified waters. Notable examples include subtropical mode waters associated with the western boundary current extensions of the subtropical gyres (the Kuroshio, Gulf Stream, East Australian, Brazil and Agulhas Currents), and the Subantarctic Mode Water forming equatorward of the ACC (Hanawa and Talley, 2001). SCVs could generate along these fronts as a result of meander-driven subduction driving low potential vorticity mode water into the stratified interior, where an anticyclonic circulation occurs due to vortex compression (Spall, 1995; Thomas, 2008). Thus, SCVs may trap mode water and propagate it far from frontal regions, potentially playing a role in mode water dispersal in the stratified interior.

Observations of SCVs from these regions show thick subsurface cores composed of homogeneous, oxygen-rich waters (Oka, 2009; Zhang et al., 2015; Xu et al., 2016; Schütte et al., 2016; Li et al., 2017; Barceló-Llull et al., 2017; Shi et al., 2018), which, along with our results, support SCVs generation by mode water subduction. Detections from Figs. 4 to 6 reveal large coherent populations of both spicy- and minty-core SCVs inhabiting the Kuroshio, East Australia, Gulf Stream, Aghulas, and Brazil Current regions (where subtropical mode waters are subducted) (Hanawa and Talley, 2001). Panel A in Fig. 14 shows representative profiles and temperature–salinity diagrams from both spicy- and minty-core SCVs detected in the vicinity of the Kuroshio extension, which closely match the results of Zhang et al.

(2015) and Li et al. (2017). These studies speculated that both spicy-and minty-core SCVs propagate through this region, and are possibly formed by frontal convergence and subduction of winter mixed-layer water along the persistent fronts of the Kuroshio. Other studies have shown that, along with large volumes of North Pacific Subtropical Mode Water (NPSTMW, $\sim 25.2~{\rm kg~m^{-3}}$), two types of North Pacific Central Mode Water (NPCMW) form between the Kuroshio Extension front and Kuroshio Bifurcation front, for a lighter variety ($\sim 25.8{-}26.2~{\rm kg~m^{-3}}$), and between the Kuroshio Bifurcation front and the Subarctic front, for a slightly denser variety ($\sim 26.3{-}26.4~{\rm kg~m^{-3}}$, Oka and Suga, 2005).

The bimodal distributions for spicy-core SCVs in the Northeast Pacific (Fig. 7) may result from subduction of both NPSTMW and the lighter NPCMW, whereas the unimodal distributions for minty-core SCVs suggest a generation along the Subarctic front from the denser NPCMW (Zhang et al., 2015). This is also supported by the more poleward occurrence of minty-core SCVs compared to spicy-core SCVs in the region. A similar mechanism may be responsible for the SCVs detected along the East Australia Current extension (Fig. 14B), which shows similar spatial patterns and vertical structures. Both spicy and minty-core SCVs with core isopycnals of approximately 26.4 kg m⁻³ are identified near the separation zone of the East Australia current, with minty-core SCVs distributed more poleward by several degrees latitude. In addition, spicy-core SCVs propagating to the north of New Zealand (Fig. 5) are co-located with the formation region for South Pacific Subtropical Mode Water (SPSTMW), exhibiting very similar characteristics to this water mass (15-19 °C, 35.5 PSU, 26.0 kg m⁻³, Hanawa and Talley, 2001).

SCVs detections along the western boundary of the Atlantic may also have connections to mode waters. North Atlantic Subtropical Mode Water (NASTMW) is characterized by temperature, salinity, and potential

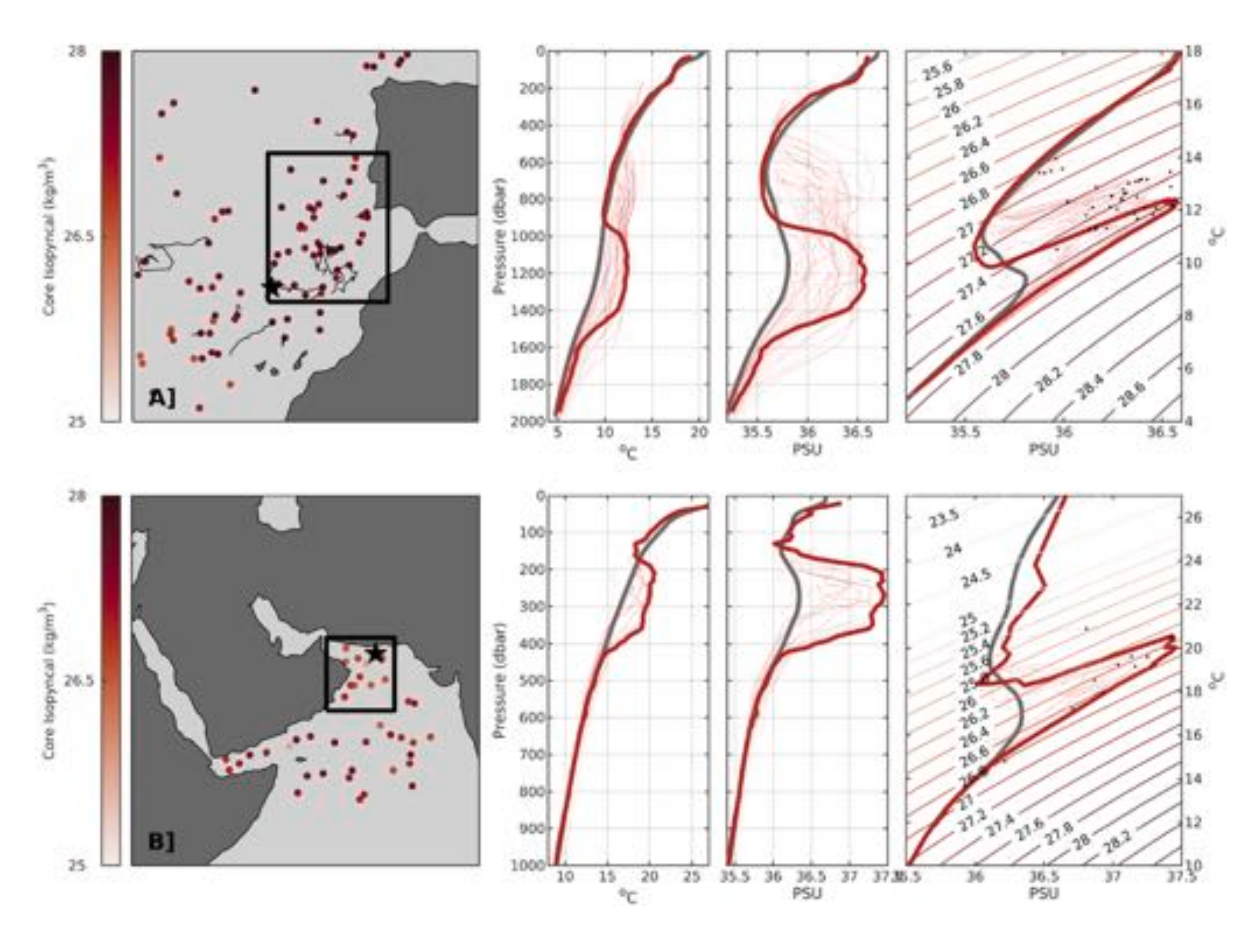


Fig. 13. (A) Locations, colored by core isopycnal, and hydrographic properties of spicy-core SCVs detected near the Mediterranean outflow. Thin black lines indicate propagation of SCVs with multiple casts. Temperature and salinity profiles and diagram are constructed from the star marker profile (Argo float 1900349, cycle 8, solid red curve), with the gray curve representing the climatological profile for that cast's location and month. Data for all other detections with the boxed region are shown as thin red lines, with black dots representing core temperature and salinity values. (B) Same as (A), but for spicy-core SCVs detected near the Gulf of Oman, with the example profile from Argo float 2902387, cycle 159. (For interpretation of the references to color in this figure legend, the reader is referred to the web version of this article.)

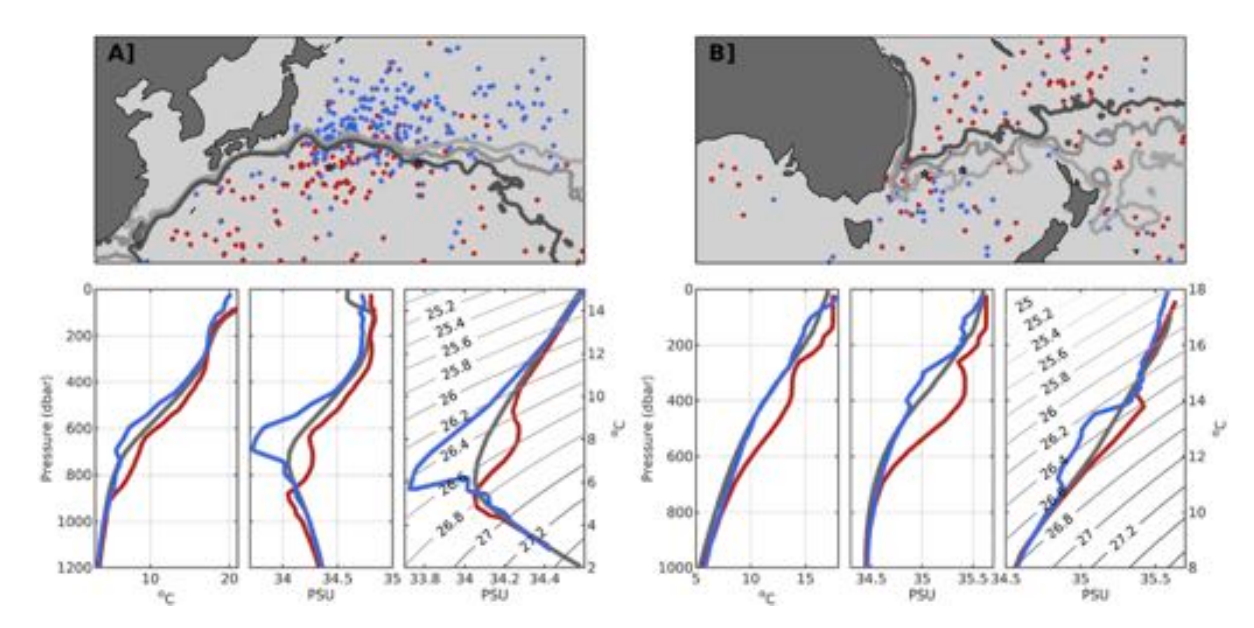


Fig. 14. (A) Locations and hydrographic properties of spicy-core (red) and minty-core (blue) SCVs detected near the Kuroshio extension. Temperature and salinity profiles and diagram are constructed from the star marker profiles for an example spicy-core SCV (Argo float 2900156, cycle 34, solid red curve) and minty-core SCV (Argo float 29010, cycle 75, solid blue curve), with the gray curve representing the climatological profile for the spicy-core SCV's location and cast month. Climatological dynamic topography contour lines (100 cm, 110 cm, and 120 cm) are also plotted. (B) Same as (A), but for spicy-core SCVs detected near the East Australia Current. The example spicy-core SCV is from Argo float 5901235, cycle 36 (red curve) and the example minty-core SCV is from Argo float 5903639, cycle 223 (blue curve); climatological dynamic topography contour lines (70 cm, 80 cm, and 90 cm) are also shown. (For interpretation of the references to color in this figure legend, the reader is referred to the web version of this article.)

PSU

density values of ~ 18 °C, 36.5 PSU, and 26.5 kg m⁻³, respectively, and is formed just south of the Gulf Stream Extension to cover the western extent of the subtropical gyre (Hanawa and Talley, 2001). Core property distributions (Fig. 8) and spatial patterns (Fig. 5) from spicy-core SCVs detected within the Northwest Atlantic match well with these characteristics, suggesting that these SCVs may form from, and eventually help spread NASTMW throughout the North Atlantic. Spatial distributions and histograms for spicy-core SCVs in the South Atlantic, with the exception of the Benguela SCVs discussed in Section 4.1, also align well with the properties and formation region of South Atlantic Subtropical Mode Water (SASTMW, 12-18 °C, 35.2-36.2 PSU, $26.2-26.6 \text{ kg m}^{-3}$).

Thus, subduction of mode waters at western boundary current fronts may be a common SCV generation mechanism throughout the western boundary of oceanic basins, just as undercurrent instabilities lead to generation along the eastern boundaries. Additionally, due to beta drift, the propagation direction would be mostly westward, which often contrasts with the large scale circulation of mode water formation regions (Shi et al., 2018). However, the process of subduction of saline subtropical surface mixed layer water is not necessarily restricted to the western extent of subtropical gyres. Nauw et al. (2006) speculated that SCV observed throughout the Indian Ocean were generated via the South Indian Tropical Front between the tropics and subtropics in the eastern part of the South Indian subtropical gyre. We also detect SCVs throughout this region, which, together with their results, suggests that other frontal structures likely generate SCVs.

Finally, a major component of the Southern Ocean overturning circulation consists of the northward export of Subantarctic Mode Water (SAMW) and Antarctic Intermediate Water (AAIW) across the Subantarctic Front—the southern boundary of the subtropical gyres, which together ventilate large areas of the lower thermocline in the Southern Hemisphere (Hanawa and Talley, 2001; Sallée et al., 2010; Cerovečki et al., 2013). SAMW forms in deep winter mixed layers poleward of the Subantarctic Front, and is characterized by wide ranges of temperature, salinity, and potential density of 4-15 °C, 34.2-35.8 PSU, and 26.5-27.1 kg m⁻³ respectively. Colder and fresher SAMW is found in the Pacific, whereas warmer and saltier waters form in the Southwestern Atlantic (Cerovečki et al., 2013).

Fig. 15 shows a typical profile from the minty-core SCVs detected along the Subantarctic Front, which exhibits a core of homogeneous temperature and salinity between roughly 400-700 dbar. Contour lines highlight the approximate locations of the Subantarctic Front (gray) and Polar Front (black) from the WOCE Southern Ocean Atlas (Orsi and Whitworth, 2005), which are poleward of the majority of mintycore SCVs detections throughout the Southern Ocean. Additionally, histograms of core temperature, salinity, and isopycnal for the mintycore SCVs of the Southern Ocean (Fig. 9), Southwest Atlantic, and Southeast Atlantic (Fig. 8) exhibit similar peaks and spread, which match hydrographic characteristics of SAMW. This result is highlighted by the similarities in mapped minty-core SCV properties throughout the high-latitude Southern Ocean (Fig. 6), suggesting a connection between these geographic regions via formation and propagation of SAMW mode water SCVs.

Previous studies have suggested that SCVs with vertically homogeneous hydrographic properties are formed at upper ocean fronts (Spall, 1995; Gordon et al., 2002; Thomas, 2008) where isopycnals from the thermocline outcrop in the winter mixed layer. At these fronts, mode waters are subducted into the thermocline, and sometimes forms isolated lenses (Nauw et al., 2006). Our results suggest that SCVs actively transport mode waters away from their formation regions. As shown in Fig. 10, ~ 1% of Argo profiles from these regions detected SCVs, highlighting a relatively high generation frequency. However, more research is needed to quantify their importance on regional and global scales. Regardless, their potential to transport recently ventilated waters may impact oxygen and nutrient budgets by periodically injecting oxygen-rich, nutrient-poor waters into the stratified interior.

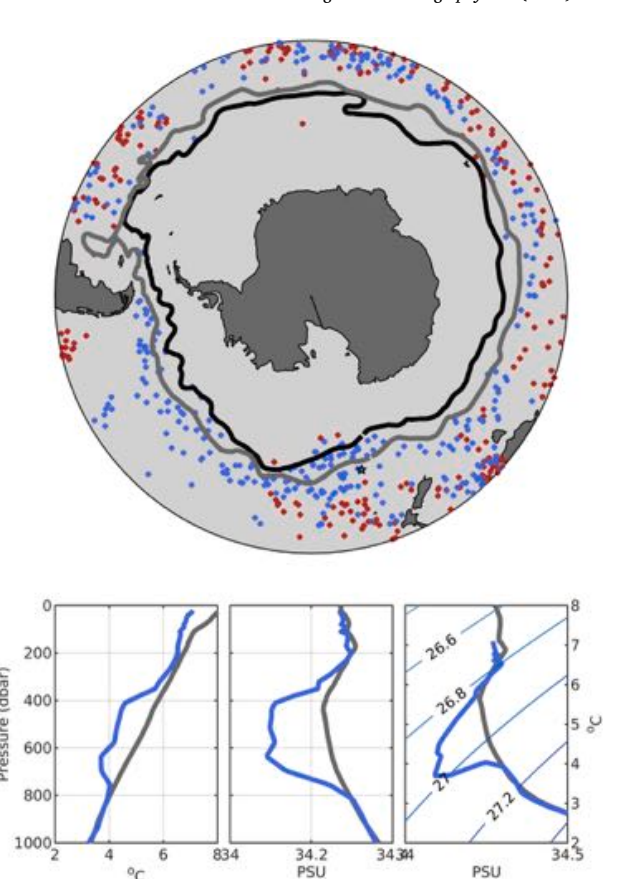


Fig. 15. Locations and hydrographic properties of spicy-core SCVs (red) and minty-core SCVs (blue) detected near the Antarctic Circumpolar Current. Contour lines represent the location of the Polar Front (black) and Subantarctic Front (gray) from the WOCE Southern Ocean Atlas (Orsi and Whitworth, 2005). Temperature and salinity profiles and diagram are constructed from the star marker profile (Argo float 1901435, cycle 217, solid blue curve), with the gray curve representing the climatological profile for that cast's location and month. (For interpretation of the references to color in this figure legend, the reader is referred to the web version of this article.)

5. SCV impacts

Our detections show regional generation of SCVs that can propagate temperature, salinity, and other tracer anomalies over basin scales, as observed for Meddies and Cuddies. To illustrate the potential to significantly modify local and remote water mass properties, we provide a first-order estimate of the heat and freshwater contributions from detectable SCVs at any given location in the ocean. To this end, we first utilize detection statistics from Fig. 10 and regional averages of SCV scale height and radius to build a simple model of SCV distribution based on scaling arguments (Appendix A and B), and use it to provide a first-order estimate of their frequency in the ocean. We then use similar scaling arguments applied to regionally averaged temperature and salinity anomalies to estimate the heat and salt content lost or gained at any given point in the ocean because of the presence of SCVs.

After dividing the ocean into 4° by 4° latitude/longitude cells, a first-order upper-bound estimate (Appendix A) of the spatial density distribution of SCVs (n_{scv} , in units of # km⁻²) can be written as

$$n_{\rm scv} = \frac{N_{\rm d}}{N_{\rm a}} \frac{1}{\pi \alpha^2 L^2} \,,\tag{7}$$

where N_d is the number of detected spicy or minty SCVs, N_a is the number of quality controlled Argo casts, L is SCV scale length (km), α is a scaling factor (here set to 1, see Appendix A), and the overbar represents the average calculated from all spicy or minty SCVs within the grid cell. Similar to (7), a first-order lower-bound estimate of the

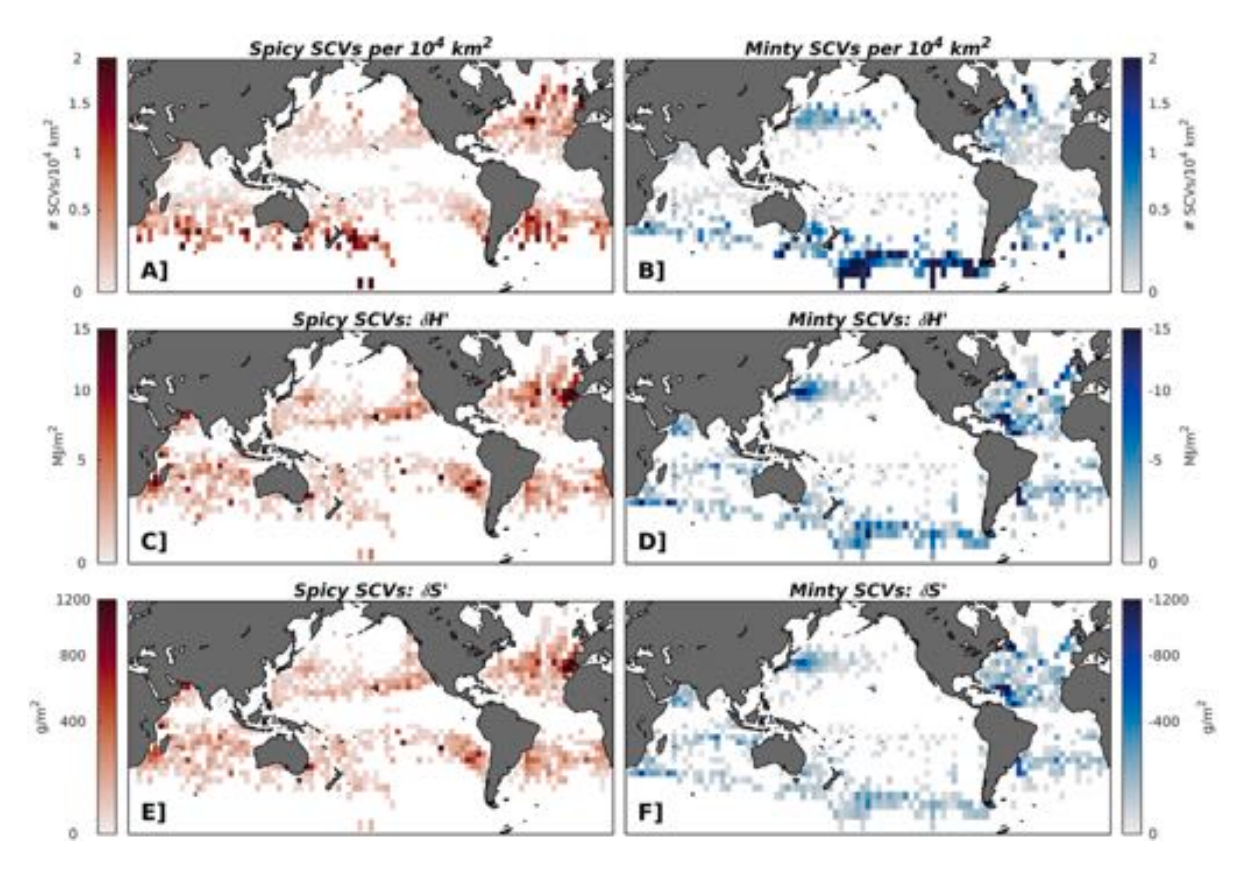


Fig. 16. (A, B) Estimate of the number of SCVs per $100 \times 100 \text{ km}^2$, derived for each $4^{\circ} \times 4^{\circ}$ longitude/latitude grid cell for spicy-core SCVs and minty-core SCVs, respectively. (C, D) Average heat anomaly caused by the presence of SCVs, $\delta H'$ (MJ m^{-2}), calculated from all spicy-core and minty-core SCVs, respectively, within each grid cell. (E, F) Average salt anomaly caused by the presence of SCVs, $\delta S'$ (g m^{-2}), calculated from all spicy-core and minty-core SCVs, respectively, within each grid cell.

average heat anomaly caused by the presence of SCVs at any given location in the ocean ($\delta H'$, in units of J m⁻², Appendix B) can be defined as

$$\delta H' = \gamma \rho C_p \frac{N_d}{N_a} \frac{\pi^{\frac{1}{2}} \overline{T'_d} h L^2}{\overline{L^2}},$$
 (8)

where γ is a scaling factor (here set to 1, see Appendix B), ρ is average ocean density (1027 kg m⁻³), $C_{\rm p}$ is the specific heat capacity of seawater (3850 J kg⁻¹° C⁻¹), $T_{\rm d}'$ is the detected core temperature anomaly (° C), and h is the SCV scale height. The salt anomaly ($\delta S'$, in units of g m⁻²) is given by

$$\delta S' = \gamma \, \rho \, \frac{N_{\rm d}}{N_{\rm a}} \, \frac{\pi^{\frac{1}{2}} \, \overline{S'_{\rm d} \, h \, L^2}}{\overline{L^2}} \,, \tag{9}$$

where S'_d is the detected core salinity anomaly (g kg⁻¹).

Fig. 16 shows the result from these equations applied to the same $4^{\circ} \times 4^{\circ}$ latitude/longitude grid shown in Fig. 10. Panels A and B provide estimates of the spatial density of spicy-core and minty-core SCVs throughout the ocean respectively. Both plots reveal increasing numbers of SCVs at higher latitudes. Many of the grid cells throughout the Southern Ocean show values of 1–2 SCVs per $100 \times 100 \text{ km}^2$; other regions with high SCV spatial density include the North Atlantic, Mediterranean outflow, and Southwest Atlantic regions for spicy-core SCVs, and the Kuroshio and Labrador Sea regions for minty-core SCVs. According to the arguments in Dewar and Meng (1995), high-latitude SCVs are expected to be smaller due to the decrease in the first baroclinic radius of deformation with latitude, which scales inversely with the Coriolis frequency (f) and linearly with the buoyancy frequency N. Thus, the area of SCVs (hence, the probability of being detected by randomly-located Argo profiles) increases with the square of the radius, which is much larger near the equator, compared to polar regions. This

makes SCVs comparably easier to detect at low latitudes, implying that the same relative number of detections at low versus high latitudes in Fig. 10 corresponds to a larger spatial density of SCVs at higher latitudes.

However, as revealed in panels C-F in Fig. 16, the relatively high spatial density observed throughout the high latitudes does not necessarily correspond to a similar amplification in anomalous heat (MJ m⁻²) and salt (g m⁻²) brought about by SCVs. Although SCVs are more frequently found in these regions, their area and volume are smaller than those observed at lower latitudes. Therefore, the higher frequency of SCVs at higher latitudes is compensated by their smaller volumes, leading to comparable heat and salt anomalies. Rather, we find that the influence of spicy-core SCVs on heat and salt peaks near the overflow regions and throughout the Pacific EBUS (Sections 4.1 and 4.2). This result is not surprising given the large temperature and salinity anomalies associated with dense, warm and salty overflow waters (Fig. 13), and the PEW advected by the California and Peru-Humboldt Undercurrents (Fig. 11). Similarly, while amplified heat and salt contributions from minty-core SCVs were co-located with high spatial densities near the Kuroshio extension, the Labrador Sea, and throughout the Southern Ocean, notable peaks were also identified off of the Caribbean region in the North Atlantic. Temperature and salinity anomalies associated with North Brazil Current subsurface eddies had been previously described by Fratantoni and Richardson (2006); our findings provide further evidence that these SCVs may play an important role on the upper ocean hydrography of this region.

Our results provide more evidence that SCV generation and propagation modify the hydrographic properties of both nearby and remote regions, in particular by spreading heat and salt from EBUS undercurrents, overflows, and mode waters. We further reveal unexpected amplifications for regions such as the Caribbean and Labrador Sea. The net transport of heat and salt by SCVs may ultimately alter the

properties of water masses as they form and decay, in turn affecting ocean circulation.

It is important to stress that the simple model on which Fig. 16 is based depends on a simplification of the real distribution, structure, and hydrographic impact of SCVs. For example, it does not consider important elements such as the life cycle of SCVs, their propagation and dissipation, and their interaction with the sampling strategy of Argo floats. It also estimates average anomalies caused by the presence of SCVs, but not by their dissipation. Furthermore, the number of detections depends on several parameters of our detection algorithm, including relatively strict IQR thresholds (Section 2.2). Thus, we are likely under sampling the true number of SCVs, and our analysis likely represents a conservative estimate on the effect of relatively strong SCVs. Regardless, it provides a first order estimate of essential quantities needed to characterize the impact of SCVs on oceanic circulation, including transport of heat and salt, and should be seen as a first step towards the development of more realistic models of the distribution of SCVs.

6. Summary

In this study, we developed a method for detecting subsurface anticyclonic eddies (SCVs) using spiciness, stratification, and dynamic height anomalies derived from Argo float profiles. By utilizing the high spatial and temporal resolution sampling provided by the nearly 4000 operational Argo floats, we detected 1716 spicy-core and 1258 minty-core SCVs in the Argo record, showing that subsurface anticyclonic eddies populate vast swaths of the global ocean. Based on the statistics of detected SCVs, we infer the location and characteristics of regional SCV populations, highlighting several hot-spots of formation that tend to generate long-lived SCVs (Figs. 4, 5, 6, and 10).

Among these, poleward undercurrents associated with EBUS and the Mediterranean outflow appear to produce abundant SCVs capable of reaching the subtropical gyres. Based on a comparison with surrounding waters, these SCVs may provide a significant source of undercurrent water to these regions, while also potentially weakening undercurrent signatures as they flow poleward. Mode water formation regions near persistent fronts associated with western boundary currents and the ACC also appear as hot-spots of SCV formation, suggesting an important role for SCVs in spreading mode waters.

Finally, we provided a first-order estimate of the number of SCVs and their contribution to heat and salt wherever they appear. Our results suggest that SCVs play a role in modulating water properties in the subtropical gyres and mid-latitude subduction regions, which in turn may alter interior water mass characteristics. Quantifying the impact of SCVs on heat, salt and tracer fluxes will benefit from a more detailed characterization of SCV frequency, movement, dissipation, and three-dimensional shape. This will likely require more accurate statistical models of the structure and life cycle of SCVs, constrained by Argo and other observations, as well as the use of high-resolution numerical models.

Declaration of competing interest

The authors declare that they have no known competing financial interests or personal relationships that could have appeared to influence the work reported in this paper.

Acknowledgments

This material is based in part upon work supported by the National Science Foundation (NSF), USA under Grants 1635632, 1847687, and 1751386. These data were collected and made freely available by the International Argo Program and the national programs that contribute to it (http://www.argo.ucsd.edu, http://argo.jcommops.org). The Argo

Program is part of the Global Ocean Observing System. The 1992–2012 mean ocean dynamic topography data has been obtained from Nikolai Maximenko (IPRC) and Peter Niiler (SIO) through the Asia-Pacific Data Research Center, which is a part of the International Pacific Research Center at the University of Hawai'i at Mānoa, funded in part by the National Oceanic and Atmospheric Administration (NOAA), USA. The spatial distributions of the Antarctic Circumpolar Current fronts from Orsi and Whitworth (2005) have been obtained from the WOCE Southern Ocean Atlas. The code utilized for the SCV detection and the datasets produced in this work are available for download through Zenodo (https://doi.org/10.5281/zenodo.4037179 and https://doi.org/10.5281/zenodo.4037442, respectively). The authors would also like to thank Victor Ciaramitaro and James Huntley for initial analysis of SCVs in Argo data.

Appendix A-D. Supplementary materials

Supplementary material related to this article can be found online at https://doi.org/10.1016/j.pocean.2020.102452. Appendices A and B detail the rationale for the methods in section 5. Appendix C provides supplementary figures. Appendix D groups regional SCV detections within each major oceanic basin to provide statistics on identified coherent populations of spicy-core and minty-core SCVs in greater detail.

References

- Altabet, M.A., Ryabenko, E., Stramma, L., Wallace, D.W., Frank, M., Grasse, P., Lavik, G., 2012. An eddy-stimulated hotspot for fixed nitrogen-loss from the Peru oxygen minimum zone. Biogeosciences http://dx.doi.org/10.5194/bg-9-4897-2012.
- Arévalo-Martínez, D.L., Kock, A., Löscher, C.R., Schmitz, R.A., Stramma, L., Bange, H.W., 2015. Influence of mesoscale eddies on the distribution of nitrous oxide in the eastern tropical South Pacific. Biogeosci. Discuss. 12 (12), 9243–9273. http://dx.doi.org/10.5194/bgd-12-9243-2015.
- Bakun, A., Nelson, C.S., 1991. The seasonal cycle of wind-stress curl in subtropical eastern boundary current regions. J. Phys. Oceanogr. 21 (12), 1815–1834. http: //dx.doi.org/10.1175/1520-0485(1991)021<1815:TSCOWS>2.0.CO;2.
- Barbosa Aguiar, A.C., Peliz, A., Carton, X., 2013. A census of Meddies in a long-term high-resolution simulation. Prog. Oceanogr. 116, 80–94. http://dx.doi.org/10.1016/ j.pocean.2013.06.016.
- Barceló-Llull, B., Sangrà, P., Pallàs-Sanz, E., Barton, E.D., Estrada-Allis, S.N., Martínez-Marrero, A., Aguiar-González, B., Grisolía, D., Gordo, C., Rodríguez-Santana, A., Marrero-Díaz, .A., Arístegui, J., 2017. Anatomy of a subtropical intrathermocline eddy. Deep Sea Res. I 124 (March), 126–139. http://dx.doi.org/10.1016/j.dsr.2017. 03.012.
- Bashmachnikov, I., Neves, F., Calheiros, T., Carton, X., 2015. Properties and pathways of Mediterranean water eddies in the Atlantic. Prog. Oceanogr. 137, 149–172. http://dx.doi.org/10.1016/j.pocean.2015.06.001.
- Bower, A.S., Armi, L., Ambar, I., 1997. Lagrangian OBservations of Meddy Formation during A Mediterranean Undercurrent Seeding Experiment. J. Phys. Oceanogr. 27 (12), 2545–2575. http://dx.doi.org/10.1175/1520-0485(1997) 027<2545:LOOMFD>2.0.CO;2.
- Bower, A.S., Furey, H.H., 2012. Mesoscale eddies in the Gulf of Aden and their impact on the spreading of Red Sea Outflow Water. Prog. Oceanogr. 96 (1), 14–39. http://dx.doi.org/10.1016/j.pocean.2011.09.003.
- Bower, A.S., Hendry, R.M., Amrhein, D.E., Lilly, J.M., 2013. Direct observations of formation and propagation of subpolar eddies into the Subtropical North Atlantic. Deep-Sea Res. II 85, 15–41. http://dx.doi.org/10.1016/j.dsr2.2012.07.029.
- Carton, X., L'Hegaret, P., Baraille, R., 2012. Mesoscale variability of water masses in the Arabian Sea as revealed by ARGO floats. Ocean Sci. 8 (2), 227–248. http://dx.doi.org/10.5194/os-8-227-2012.
- Cerovečki, I., Talley, L.D., Mazloff, M.R., Maze, G., 2013. Subantarctic Mode Water Formation, Destruction, and Export in the Eddy-Permitting Southern Ocean State Estimate. J. Phys. Oceanogr. 43 (7), 1485–1511. http://dx.doi.org/10.1175/JPO-D-12-0121.1.
- Chaigneau, A., Le Texier, M., Eldin, G., Grados, C., Pizarro, O., 2011. Vertical structure of mesoscale eddies in the eastern South Pacific Ocean: A composite analysis from altimetry and Argo profiling floats. J. Geophys. Res.: Oceans 116 (C11), http://dx.doi.org/10.1029/2011JC007134.
- Chavez, F.P., Messié, M., 2009. A comparison of Eastern Boundary Upwelling Ecosystems. Prog. Oceanogr. 83 (1–4), 80–96. http://dx.doi.org/10.1016/j.pocean.2009. 07.032

- Chelton, D.B., DeSzoeke, R.A., Schlax, M.G., El Naggar, K., Siwertz, N., 1998. Geographical Variability of the First Baroclinic Rossby Radius of Deformation. J. Phys. Oceanogr. 28 (3), 433–460. http://dx.doi.org/10.1175/1520-0485(1998) 028<0433:GVOTFB>2.0.CO;2.
- Colas, F., McWilliams, J.C., Capet, X., Kurian, J., McWilliams, J.C., Capet, X., Kurian, J., 2012. Heat balance and eddies in the Peru-Chile current system. Clim. Dynam. 39 (1–2), 509–529. http://dx.doi.org/10.1007/s00382-011-1170-6.
- Collins, C.A., Margolina, T., Rago, T.A., Ivanov, L., 2013. Looping RAFOS floats in the California Current System. Deep-Sea Res. II 85, 42–61. http://dx.doi.org/10.1016/ j.dsr2.2012.07.027.
- Combes, V., Hormazabal, S., Di Lorenzo, E., 2015. Interannual variability of the subsurface eddy field in the Southeast Pacific. J. Geophys. Res. C: Oceans 120 (7), 4907–4924. http://dx.doi.org/10.1002/2014JC010265.
- Cushman-Roisin, B., Beckers, J.-M., 2011. Introduction to Geophysical Fluid Dynamics. International Geophysics, second ed. Elsevier Ltd, San Diego, p. 875.
- D'Asaro, E.A., 1988. Generation of submesoscale vortices: A new mechanism. J. Geophys. Res. 93 (C6), 6685. http://dx.doi.org/10.1029/JC093iC06p06685.
- de Boyer Montégut, C., Madec, G., Fischer, A.S., Lazar, A., Iudicone, D., 2004. Mixed layer depth over the global ocean: An examination of profile data and a profilebased climatology. J. Geophys. Res. C: Oceans 109 (12), 1–20. http://dx.doi.org/ 10.1029/2004JC002378.
- Dewar, W.K., McWilliams, J.C., Molemaker, M.J., 2015. Centrifugal Instability and Mixing in the California Undercurrent. J. Phys. Oceanogr. 45 (5), 1224–1241. http://dx.doi.org/10.1175/JPO-D-13-0269.1.
- Dewar, W.K., Meng, H., 1995. The Propagation of Submesoscale Coherent Vortices. J. Phys. Oceanogr. 25 (8), 1745–1770. http://dx.doi.org/10.1175/1520-0485(1995) 025<1745:TPOSCV>2.0.CO;2.
- Dilmahamod, A.F., Aguiar-González, B., Penven, P., Reason, C.J.C., De Ruijter, W.P.M., Malan, N., Hermes, J.C., 2018. SIDDIES COrridor: A Major East-West Pathway of Long-Lived Surface and Subsurface Eddies Crossing the Subtropical South Indian Ocean. J. Geophys. Res.: Oceans 123 (8), 5406–5425. http://dx.doi.org/10.1029/ 2018JC013828.
- Fratantoni, D.M., Richardson, P.L., 2006. The evolution and demise of North Brazil Current rings. J. Phys. Oceanogr. 36 (7), 1241–1264. http://dx.doi.org/10.1175/JPO2907.1.
- Frenger, I., Bianchi, D., Stührenberg, C., Oschlies, A., Dunne, J., Deutsch, C., Galbraith, E., Schütte, F., 2018. Biogeochemical Role of Subsurface Coherent Eddies in the Ocean: Tracer Cannonballs, Hypoxic Storms, and Microbial Stewpots? Glob. Biogeochem. Cycles 32 (2), 226–249. http://dx.doi.org/10.1002/2017GB005743.
- Garfield, N., Collins, C.A., Paquette, R.G., Carter, E., 1999. Lagrangian EXploration of the California Undercurrent, 1992–95. J. Phys. Oceanogr. 29 (4), 560–583. http://dx.doi.org/10.1175/1520-0485(1999)029<0560:LEOTCU>2.0.CO;2.
- Gaube, P., McGillicuddy, D.J., Moulin, A.J., 2018. Mesoscale Eddies Modulate Mixed Layer Depth Globally. Geophys. Res. Lett. http://dx.doi.org/10.1029/ 2018GL080006
- Gill, A., 1982. Atmosphere-Ocean Dynamics. Academic Press, New York, p. 662.
- Gordon, A.L., Giulivi, C.F., Lee, C.M., Furey, H.H., Bower, A., Talley, L., 2002. Japan/East Sea Intrathermocline Eddies. J. Phys. Oceanogr. 32 (6), 1960–1974. http://dx.doi.org/10.1175/1520-0485(2002)032<1960:jesie>2.0.co;2.
- Grundle, D.S., Löscher, C.R., Krahmann, G., Altabet, M.A., Bange, H.W., Karstensen, J., Körtzinger, A., Fiedler, B., 2017. Low oxygen eddies in the eastern tropical North Atlantic: Implications for N₂O cycling. Sci. Rep. 7 (1), 1–10. http://dx.doi.org/10. 1038/s41598-017-04745-y.
- Hanawa, K., Talley, L., 2001. Chapter 5.4 Mode waters. Int. Geophys. 77, 373–386. http://dx.doi.org/10.1016/S0074-6142(01)80129-7.
- Hauss, H., Christiansen, S., Schütte, F., Kiko, R., Edvam Lima, M., Rodrigues, E., Karstensen, J., Löscher, C.R., Körtzinger, A., Fiedler, B., 2016. Dead zone or oasis in the open ocean? Zooplankton distribution and migration in low-oxygen modewater eddies. Biogeosciences 13 (6), 1977–1989. http://dx.doi.org/10.5194/bg-13-1977-2016
- Hogan, P., Hurlburt, H., 2011. Why do Intrathermocline Eddies Form in the Japan/East Sea? A Modeling Perspective. Oceanography 19 (3), 134–143. http://dx.doi.org/10. 5670/oceanog.2006.50.
- Hormazabal, S., Combes, V., Morales, C.E., Correa-Ramirez, M.A., Di Lorenzo, E., Nuñez, S., 2013. Intrathermocline eddies in the coastal transition zone off central Chile (31–41°S). J. Geophys. Res.: Oceans 118 (10), 4811–4821. http://dx.doi.org/ 10.1002/jgrc.20337.
- Johnson, G.C., McTaggart, K.E., 2010. Equatorial Pacific 13°C Water Eddies in the Eastern Subtropical South Pacific Ocean. J. Phys. Oceanogr. http://dx.doi.org/10. 1175/2009JPO4287 1
- Kämpf, J., Chapman, P., 2016. Upwelling systems of the world: A scientific journey to the most productive marine ecosystems. In: Upwelling Systems of the World: A Scientific Journey to the Most Productive Marine Ecosystems. pp. 1–433. http: //dx.doi.org/10.1007/978-3-319-42524-5.
- Karstensen, J., Fiedler, B., Schütte, F., Brandt, P., Körtzinger, A., Fischer, G., Zantopp, R., Hahn, J., Visbeck, M., Wallace, D., 2015. Open ocean dead zones in the tropical North Atlantic Ocean. Biogeosciences 12 (8), 2597–2605. http://dx.doi.org/10.5194/bg-12-2597-2015.

- Karstensen, J., Schütte, F., Pietri, A., Krahmann, G., Fiedler, B., Grundle, D., Hauss, H., Körtzinger, A., Löscher, C.R., Testor, P., Vieira, N., Visbeck, M., 2017. Upwelling and isolation in oxygen-depleted anticyclonic modewater eddies and implications for nitrate cycling. Biogeosciences 14 (8), 2167–2181. http://dx.doi.org/10.5194/ bg-14-2167-2017.
- Klenz, T., Dengler, M., Brandt, P., 2018. Seasonal Variability of the Mauritania Current and Hydrography at 18°N. J. Geophys. Res.: Oceans 123 (11), 8122–8137. http: //dx.doi.org/10.1029/2018JC014264.
- Lass, H.U., Mohrholz, V., 2008. On the interaction between the subtropical gyre and the Subtropical Cell on the shelf of the SE Atlantic. J. Mar. Syst. http://dx.doi.org/ 10.1016/j.imarsvs.2007.09.008.
- Lass, H.U., Schmidt, M., Mohrholz, V., Nausch, G., 2000. Hydrographic and current measurements in the area of the Angola–Benguela Front. J. Phys. Oceanogr. http://dx.doi.org/10.1175/1520-0485(2000)030<2589:HACMIT>2.0.CO;2.
- Legg, S., Briegleb, B., Chang, Y., Chassignet, E.P., Danabasoglu, G., Ezer, T., Gordon, A.L., Griffies, S., Hallberg, R., Jackson, L., Large, W., Özgükmen, T.M., Peters, H., Price, J., Riemenschneider, U., Wu, W., Xu, X., Yang, J., 2009. Improving oceanic overflow representation in climate models: The Gravity Current Entrainment Climate Process Team. Bull. Am. Meteorol. Soc. 90 (5), 657–670. http://dx.doi.org/10.1175/2008BAMS2667.1.
- L'Hégaret, P., Carton, X., Louazel, S., Boutin, G., 2016. Mesoscale eddies and submesoscale structures of Persian Gulf Water off the Omani coast in spring 2011. Ocean Sci. 12 (3), 687–701. http://dx.doi.org/10.5194/os-12-687-2016.
- Li, C., Zhang, Z., Zhao, W., Tian, J., 2017. A statistical study on the subthermocline submesoscale eddies in the northwestern Pacific Ocean based on Argo data. J. Geophys. Res.: Oceans 122 (5), 3586–3598. http://dx.doi.org/10.1002/2016JC012561.
- Löscher, C.R., Fischer, M.A., Neulinger, S.C., Fiedler, B., Philippi, M., Schütte, F., Singh, A., Hauss, H., Karstensen, J., Körtzinger, A., Künzel, S., Schmitz, R.A., 2015. Hidden biosphere in an oxygen-deficient Atlantic open ocean eddy: Future implications of ocean deoxygenation on primary production in the eastern tropical North Atlantic. Biogeosci. Discuss. 12 (16), 14175–14213. http://dx.doi.org/10.5194/bgd-12-14175-2015.
- Lukas, R., Santiago-Mandujano, F., 2001. Extreme water mass anomaly observed in the Hawaii ocean time-series. Geophys. Res. Lett. 28 (15), 2931–2934. http://dx.doi. org/10.1029/2001GL013099.
- Lynn, R.J., Simpson, J.J., 1987. The California Current System: The seasonal variability of its physical characteristics. J. Geophys. Res.: Oceans http://dx.doi.org/10.1029/ JC092iC12p12947, (1978–2012).
- McGillicuddy, D.J., 2014. Formation of Intrathermocline Lenses by Eddy-Wind Interaction. J. Phys. Oceanogr. 45 (2), 606-612. http://dx.doi.org/10.1175/jpo-d-14-0221.1.
- McWilliams, J.C., 1985. Submesoscale, coherent vortices in the ocean. Rev. Geophys. 23 (2), 165. http://dx.doi.org/10.1029/RG023i002p00165.
- McWilliams, J.C., 2019. A survey of submesoscale currents. Geosci. Lett. 6 (1), http://dx.doi.org/10.1186/s40562-019-0133-3.
- Ménesguen, C., Hua, B.L., Carton, X., Klingelhoefer, F., Schnürle, P., Reichert, C., 2012. Arms winding around a meddy seen in seismic reflection data close to the Morocco coastline. Geophys. Res. Lett. 39 (5), n/a-n/a. http://dx.doi.org/10.1029/ 2011GI.050798
- Meunier, T., Tenreiro, M., Pallàs-Sanz, E., Ochoa, J., Ruiz-Angulo, A., Portela, E., Cusí, S., Damien, P., Carton, X., 2018. Intrathermocline Eddies Embedded Within an Anticyclonic Vortex Ring. Geophys. Res. Lett. 45 (15), 7624–7633. http://dx.doi.org/10.1029/2018GI.077527.
- Mohrholz, V., Schmidt, M., Lutjeharms, J.R., 2001. The hydrography and dynamics of the Angola-Benguela Frontal Zone and environment in April 1999. S. Afr. J. Sci..
- Molemaker, M.J., McWilliams, J.C., Dewar, W.K., 2015. Submesoscale Instability and Generation of Mesoscale Anticyclones near a Separation of the California Undercurrent. J. Phys. Oceanogr. 45 (3), 613–629. http://dx.doi.org/10.1175/JPO-D-13-0225.1.
- Morvan, M., L'hégaret, P., Carton, X., Gula, J., Vic, C., De Marez, C., Sokolovskiy, M., Koshel, K., 2019. The life cycle of submesoscale eddies generated by topographic interactions. Ocean Sci. 15 (6), 1531–1543. http://dx.doi.org/10.5194/os-15-1531-2019.
- Nauw, J.J., van Aken, H.M., Lutjeharms, J.R., de Ruijter, W.P., 2006. Intrathermocline eddies in the Southern Indian Ocean. J. Geophys. Res.: Oceans 111 (3), 1–14. http://dx.doi.org/10.1029/2005JC002917.
- Oka, E., 2009. Seasonal and interannual variation of North Pacific Subtropical Mode Water in 2003–2006. J. Oceanogr. 65 (2), 151–164. http://dx.doi.org/10.1007/s10872-009-0015-y.
- Oka, E., Suga, T., 2005. Differential formation and circulation of North Pacific Central Mode Water. J. Phys. Oceanogr. 35 (11), 1997–2011. http://dx.doi.org/10.1175/JPO2811.1.
- Ollitrault, M., Colin de Verdière, A., 2014. The Ocean General Circulation near 1000-m Depth. J. Phys. Oceanogr. 44 (1), 384–409. http://dx.doi.org/10.1175/JPO-D-13-030.1.
- Orsi, A.H., Whitworth, T., 2005. Hydrographic Atlas of the World Ocean Circulation Experiment (WOCE) Vol. 1: Southern Ocean, Vol. 1. International WOCE Project Office, Southampton, U.K..
- Pegliasco, C., Chaigneau, A., Morrow, R., 2015. Main eddy vertical structures observed in the four major Eastern Boundary Upwelling Systems. J. Geophys. Res.: Oceans 120 (9), 6008–6033. http://dx.doi.org/10.1002/2015JC010950.

- Pelland, N.A., Eriksen, C.C., Lee, C.M., 2013. Subthermocline Eddies over the Washington Continental Slope as Observed by Seagliders, 2003–09. J. Phys. Oceanogr. http://dx.doi.org/10.1175/JPO-D-12-086.1.
- Radko, T., Sisti, C., 2017. Life and demise of intrathermocline mesoscale vortices. J. Phys. Oceanogr. 47 (12), 3087–3103. http://dx.doi.org/10.1175/JPO-D-17-0044.1.
- Richardson, P., Bower, A., Zenk, W., 2000. A census of Meddies tracked by floats. Prog. Oceanogr. 45 (2), 209–250. http://dx.doi.org/10.1016/S0079-6611(99)00053-1.
- Roemmich, D., Gilson, J., 2009. The 2004-2008 mean and annual cycle of temperature, salinity, and steric height in the global ocean from the Argo Program. Prog. Oceanogr. http://dx.doi.org/10.1016/j.pocean.2009.03.004.
- Sallée, J.-B., Speer, K., Rintoul, S., Wijffels, S., 2010. Southern Ocean Thermocline Ventilation. J. Phys. Oceanogr. 40 (3), 509–529. http://dx.doi.org/10.1175/2009JP04291.1
- Schneider, W., Fuenzalida, R., Rodríguez-Rubio, E., Garcés-Vargas, J., Bravo, L., 2003. Characteristics and formation of Eastern South Pacific Intermediate Water. Geophys. Res. Lett. 30 (11), 1–4. http://dx.doi.org/10.1029/2003GL017086.
- Schütte, F., Brandt, P., Karstensen, J., 2016. Occurrence and characteristics of mesoscale eddies in the tropical northeastern Atlantic Ocean. Ocean Sci. 12 (3), 663–685. http://dx.doi.org/10.5194/os-12-663-2016.
- Shapiro, G., Meschanov, S., 1991. Distribution and spreading of Red Sea Water and salt lens formation in the northwest Indian Ocean. Deep Sea Res. A 38 (1), 21–34. http://dx.doi.org/10.1016/0198-0149(91)90052-H.
- Shi, F., Luo, Y., Xu, L., 2018. Volume and Transport of Eddy-Trapped Mode Water South of the Kuroshio Extension. J. Geophys. Res.: Oceans 123 (12), 8749–8761. http://dx.doi.org/10.1029/2018JC014176.
- Siegfried, L., Schmidt, M., Mohrholz, V., Pogrzeba, H., Nardini, P., Böttinger, M., Scheuermann, G., 2019. The tropical-subtropical coupling in the Southeast Atlantic from the perspective of the northern Benguela upwelling system. PLoS One 14 (1), e0210083. http://dx.doi.org/10.1371/journal.pone.0210083.
- Simpson, J., Dickey, T., Koblinsky, C., 1984. An offshore eddy in the California Current System Part i: Interior dynamics. Prog. Oceanogr. 13 (1), 5–49. http://dx.doi.org/10.1016/0079-6611(84)90004-1.
- Simpson, J.J., Lynn, R.J., 1990. A mesoscale eddy dipole in the offshore California Current. J. Geophys. Res. 95 (C8), 13009. http://dx.doi.org/10.1029/JC095iC08p13009.
- Southwick, O.R., Johnson, E.R., McDonald, N.R., 2016. A simple model for sheddies: Ocean eddies formed from shed vorticity. J. Phys. Oceanogr. 46 (10), 2961–2979. http://dx.doi.org/10.1175/JPO-D-15-0251.1.
- Spall, M.A., 1995. Frontogenesis, subduction, and cross-front exchange at upper ocean fronts. J. Geophys. Res. 100 (C2), 2543–2557. http://dx.doi.org/10.1029/ 94JC02860
- Steinberg, J.M., Pelland, N.A., Eriksen, C.C., 2018. Observed Evolution of a California Undercurrent Eddy. J. Phys. Oceanogr. 49 (3), 649–674. http://dx.doi.org/10. 1175/jpo-d-18-0033.1.
- Szuts, Z.B., Blundell, J.R., Chidichimo, M.P., Marotzke, J., 2012. A vertical-mode decomposition to investigate low-frequency internal motion across the Atlantic at 26 N. Ocean Sci. 8 (3), 345–367. http://dx.doi.org/10.5194/os-8-345-2012.

- Talley, L.D., Pickard, G.L., Emery, W.J., Swift, J.H., 2011. Descriptive Physical Oceanography. Descriptive Physical Oceanography: An Introduction: Sixth Edition, sixth ed. Elsevier, p. 560. http://dx.doi.org/10.1016/C2009-0-24322-4.
- Thomas, L.N., 2008. Formation of intrathermocline eddies at ocean fronts by wind-driven destruction of potential vorticity. Dyn. Atmos. Oceans 45 (3–4), 252–273. http://dx.doi.org/10.1016/j.dynatmoce.2008.02.002.
- Thomas, A.C., Brickley, P., Weatherbee, R., 2009. Interannual variability in chlorophyll concentrations in the Humboldt and California Current Systems. Prog. Oceanogr. 83 (1–4), 386–392. http://dx.doi.org/10.1016/j.pocean.2009.07.020.
- Thomsen, S., Kanzow, T., Krahmann, G., Greatbatch, R.J., Dengler, M., Lavik, G., 2016. The formation of a subsurface anticyclonic eddy in the Peru-Chile Undercurrent and its impact on the near-coastal salinity, oxygen, and nutrient distributions. J. Geophys. Res.: Oceans 121 (1), 476–501. http://dx.doi.org/10.1002/2015JC010878.
- Thomsen, S., Karstensen, J., Kiko, R., Krahmann, G., Dengler, M., Engel, A., 2019. Remote and local drivers of oxygen and nitrate variability in the shallow oxygen minimum zone off Mauritania in June 2014. Biogeosciences 16 (5), 979–998. http://dx.doi.org/10.5194/bg-16-979-2019.
- Thomson, R.E., Krassovski, M.V., 2010. Poleward reach of the California Undercurrent extension. J. Geophys. Res. 115 (C9), C09027. http://dx.doi.org/10.1029/2010JC006280.
- Tukey, J.W., 1977. Exploratory Data Analysis. Addison-Wesley.
- Vic, C., Roullet, G., Capet, X., Carton, X., Molemaker, M.J., Gula, J., 2015. Eddy-topography interactions and the fate of the Persian Gulf Outflow. J. Geophys. Res.: Oceans 120 (10), 6700–6717. http://dx.doi.org/10.1002/2015JC011033.
- Warren, B.A., Wunsch, C., 1981. Evolution of physical oceanography; scientific surveys in honor of Henry Stommel. http://dx.doi.org/10.1029/eo063i019p00499-02.
- Wunsch, C., 1997. The Vertical Partition of Oceanic Horizontal Kinetic Energy. J. Phys. Oceanogr. http://dx.doi.org/10.1175/1520-0485(1997)027<1770:TVPOOH>
- Xu, L., Li, P., Xie, S.-P., Liu, Q., Liu, C., Gao, W., 2016. Observing mesoscale eddy effects on mode-water subduction and transport in the North Pacific. Nature Commun. 7 (1), 10505. http://dx.doi.org/10.1038/ncomms10505.
- Zhang, Z., Li, P., Xu, L., Li, C., Zhao, W., Tian, J., Qu, T., 2015. Subthermocline eddies observed by rapid-sampling Argo floats in the subtropical northwestern Pacific Ocean in Spring 2014. Geophys. Res. Lett. 42 (15), 6438–6445. http: //dx.doi.org/10.1002/2015GL064601.
- Zhang, Z., Zhang, Y., Wang, W., 2017. Three-compartment structure of subsurface-intensified mesoscale eddies in the ocean. J. Geophys. Res.: Oceans http://dx.doi.org/10.1002/2016JC012376.
- Zhao, M., Timmermans, M.L., Krishfield, R., Manucharyan, G., 2018. Partitioning of Kinetic Energy in the Arctic Ocean's Beaufort Gyre. J. Geophys. Res.: Oceans http://dx.doi.org/10.1029/2018JC014037.